The Journal of Physiology

When NCX switches sides: Experimental and computational insights into Ca^{2+} regulation in the heart

Wilhelm Neubert[1], Judith Hüttemeister[2], Paulina Sander[2], Nagaiah Chamakuri[3], Felix Hohendanner[2], Martin Falcke[1,4] and Frank R. Heinzel[5]

[1] *Max Delbrück Center for Molecular Medicine, Berlin, Germany*
[2] *Department of Cardiology, Deutsches Herzzentrum der Charité, Angiology and Intensive Care Medicine, Berlin, Germany*
[3] *School of Mathematics & Center for HPC, Indian Institute of Science Education and Research Thiruvananthapuram, Thiruvananthapuram, India*
[4] *Department of Physics, Humboldt University, Berlin, Germany*
[5] *2. Medizinische Klinik für Kardiologie, Angiologie, Intensivmedizin, Städtisches Klinikum Dresden, Dresden, Germany*

Handling Editor: Eleonora Grandi

The peer review history is available in the Supporting information section of this article (https://doi.org/10.1113/JP290207#support-information-section).

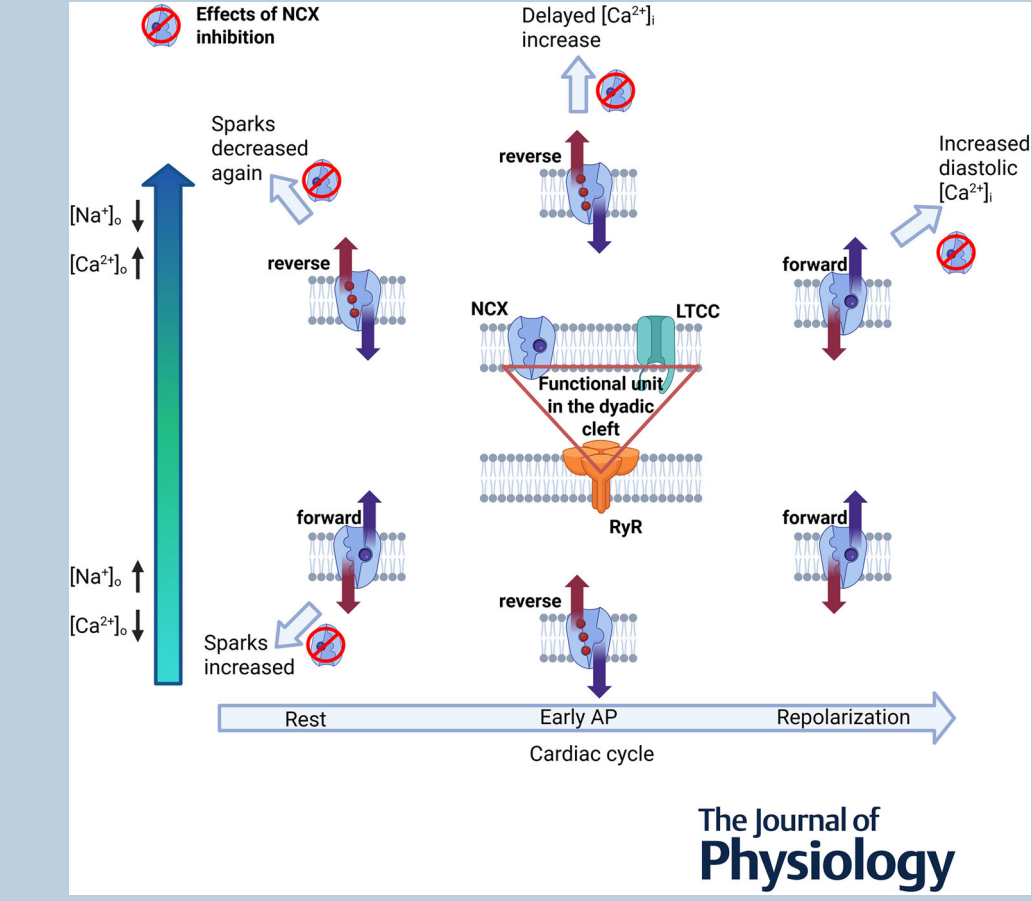

Abstract figure legend Due to its presence inside the dyadic cleft, Na^+/Ca^{2+} exchanger (NCX) builds a functional unit together with L-type calcium channels and ryanodine receptors in the dyadic cleft. NCX acts bidirectionally (forward and reverse mode) dependent on extracellular calcium ($[Ca^{2+}]_o$) and sodium ($[Na^+]_o$) concentrations and the membrane

W. Neubert & J. Hüttemeister shared first authorship

DOI: 10.1113/JP290207

potential (phase of the cardiac cycle). At low $[Ca^{2+}]_o$ and high $[Na^+]_o$, NCX acts in forward mode at rest, helping thereby to maintain cytosolic Ca^{2+} ($[Ca^{2+}]_i$) low. Inhibiting NCX causes an increase in spark frequency under these conditions as triggering $[Ca^{2+}]_i$ increases. If $[Ca^{2+}]_o$ is increased and/or $[Na^+]_o$ decreased on the other hand, NCX acts in reverse mode at rest, increasing spark frequency that can then be reduced again by inhibiting NCX. During the early phase of action potential, when $[Na^+]_i$ is already increased, NCX acts in reverse mode independent of the tested extracellular ion concentrations. This accelerates transsarcolemmal Ca^{2+} influx, as early $[Ca^{2+}]_i$ increase is delayed with NCX inhibition. When $[Ca^{2+}]_i$ rises during the cardiac cycle, NCX shifts to forward mode and supports Ca^{2+} extrusion. Overall, inhibiting NCX leads over time to an increase in diastolic $[Ca^{2+}]_i$. Created in BioRender. Hüttemeister, J. (2025).

Abstract The Na^+/Ca^{2+} exchanger (NCX) transports Ca^{2+} and Na^+ through the plasma membrane of cardiomyocytes. NCX dysregulation has been related to diastolic dysfunction. NCX inhibition has been identified as a potential therapeutic approach. It can accelerate the decay of the cytosolic Ca^{2+} concentration ($[Ca^{2+}]_i$) and improve impaired cardiomyocyte relaxation. We hypothesized that this counterintuitive effect is explained by the subcellular arrangement of NCX and local ion gradients within the intracellular Ca^{2+} release units. In a parallel model-based and experimental approach, we re-evaluated the location of NCX with regard to the dyadic cleft and its role in modulating $[Ca^{2+}]_i$. Stimulated emission depletion imaging revealed NCX in close proximity to junctophilin (the marker for the dyadic cleft). We simulated $[Ca^{2+}]$ dynamics in the dyadic cleft considering Ca^{2+} channels, NCX molecules and local concentration gradients. Positioning NCX inside the dyadic cleft in our computational model matched its action on spark rate. In forward mode (Ca^{2+} out, Na^+ in) NCX decreased spontaneous Ca^{2+} release events (spark rate) in simulations and imaging experiments, while in reverse mode it increased them. In paced cardiomyocytes, NCX inhibition consistently increased diastolic $[Ca^{2+}]$. The effects of NCX inhibition on transient amplitude and peak, however, depended on extracellular $[Ca^{2+}]_o$ suggesting a role of reverse-mode NCX activity at high $[Ca^{2+}]_o$. NCX inhibition prolonged the early rise of $[Ca^{2+}]$, corroborating that reverse-mode NCX facilitates the rapid initial increase of $[Ca^{2+}]_i$ during excitation. Our combined imaging, modelling and functional data support the hypothesis that NCX resides in the dyadic cleft where it bidirectionally shapes Ca^{2+} transients and spark activity.

(Received 1 October 2025; accepted after revision 16 March 2026; first published online 4 April 2026)
Corresponding authors M. Falcke: Max Delbrück Center for Molecular Medicine, Robert Rössle Str. 10, 13092 Berlin, Germany. Email: Martin.Falcke@mdc-berlin.de
F. R. Heinzel: 2. Medizinische Klinik für Kardiologie, Angiologie, Intensivmedizin. Städtisches Klinikum Dresden, Friedrichstraße 41, 01067 Dresden, Germany. Email: Frank.Heinzel@klinikum-dresden.de

Key points

- Our data suggest that Na^+/Ca^{2+} exchanger (NCX) is localized inside the dyadic cleft in cardiomyocytes, close to junctophilin, as shown by stimulated emission depletion imaging.
- Computational modelling confirmed NCX's dyadic positioning. It is critical for its effects on local Ca^{2+} signalling.
- NCX bidirectionally modulates Ca^{2+} dynamics: forward mode reduces, reverse mode increases spontaneous Ca^{2+} sparks.
- NCX inhibition raises diastolic cytosolic Ca^{2+} and alters Ca^{2+} transient amplitude depending on extracellular Ca^{2+} levels.
- Reverse-mode NCX facilitates rapid initial Ca^{2+} rise during excitation, highlighting its role in cardiac Ca^{2+} regulation and potential therapy.

Introduction

Excitation–contraction coupling (ECC) links electrical activation to intracellular Ca^{2+} cycling, thereby supporting normal cardiac function and functional reserve; maladaptation of this system during cardiac remodelling contributes to both mechanical dysfunction and arrhythmias (Landstrom et al., 2017). Defective ECC in hypertrophy and heart failure has long been framed as a disturbance of local coupling geometry between sarcolemmal Ca^{2+} entry and sarcoplasmic reticulum (SR) Ca^{2+} release rather than a simple loss of channels (Gomez et al., 1997). Within this framework, the Na^+/Ca^{2+} exchanger (NCX) is a key modulator of Ca^{2+} balance and contractile performance and can also contribute to Ca^{2+} entry depending on transmembrane gradients and membrane voltage (Gaughan et al., 1999; Ottolia et al., 2013). Despite extensive work, how NCX's microdomain positioning shapes its net impact on ECC and arrhythmogenesis remains incompletely understood (Landstrom et al., 2017).

During the cardiac cycle, Ca^{2+} is released from specialized microdomains known as calcium release units (CRUs) comprising also the dyadic cleft, where the SR comes into close proximity with the cell membrane along the T-tubule network. There are two main types of channel within CRUs: the voltage gated plasma membrane L-type Ca^{2+} channel (LCC) on the cell membrane and the Ca^{2+}-sensitive ryanodine receptor (RyR) channels on the SR membrane. LCCs open and allow a small amount of Ca^{2+} into the dyadic space upon membrane potential depolarization. The locally increased Ca^{2+} concentration causes RyRs to open and release a much larger amount of Ca^{2+} from the SR into the cytosol. This process is called calcium-induced calcium release (CICR). The released Ca^{2+} diffuses throughout the cytosol and binds to troponin C, initiating myocyte contraction. The release of Ca^{2+} from a RyR cluster can also occur spontaneously in isolated CRUs, triggered by the random opening of the first RyR in the cluster. Such spontaneous release events are called sparks. Importantly, since sparks do not depend on an active action potential to occur, they allow for insights into local release behaviour.

Cytosolic $[Ca^{2+}]$ increases during the action potential due to influx through the LCCs and release of Ca^{2+} from the SR. $[Ca^{2+}]$ decays in physiological conditions mainly due to SR Ca^{2+}-ATPase (SERCA)-mediated Ca^{2+} reuptake into the SR, by the plasma membrane Ca^{2+}-ATPase and by the plasma membrane Na^+/Ca^{2+} exchanger (NCX), which transports three Na^+ ions into the cell for every Ca^{2+} ion extruded to overcome the electrochemical gradient of Ca^{2+} across the cell membrane (Blaustein & Lederer, 1999). Both the LCC and the NCX couple $[Ca^{2+}]$ dynamics to the membrane voltage V_m. NCX works in forward (Ca^{2+} out, Na^+ in) or reverse mode depending on local (sub-plasma membrane) ion concentrations (Tanaka et al., 2007) and NCX regulation by membrane voltage. Several changes of direction during the normal action potential may occur (Bouchard et al., 1993; Ottolia et al., 2013).

Studies on the role of NCX in heart failure with preserved ejection fraction (HFpEF) related it to diastolic dysfunction (Correia Pinto et al., 2006; De Angelis et al., 2016; Kamimura et al., 2012; Primessnig et al., 2016; Rouhana et al., 2019) and identified NCX inhibition as a potential therapeutic approach, but at the same time emphasized the quantitatively complex interaction of the NCX with other Ca^{2+} transporters in the cardiomyocyte. Diastolic dysfunction in HFpEF animal models was related to a decreased cytosolic Ca^{2+} extrusion via the NCX. Acute inhibition of NCX using selective inhibitors such as SEA0400 and ORM-11035 has demonstrated significant improvements in diastolic function, including accelerated Ca^{2+} transient decay, decreased spontaneous Ca^{2+} release (Primessnig et al., 2016) and normalization of relaxation parameters without negatively impacting systolic Ca^{2+} transient amplitude or SR Ca^{2+} content. Particularly, the effect of NCX inhibition on transient decay is surprising and not fully understood.

A precise understanding of NCX function is highly relevant, since its bidirectional activity may directly affect $[Ca^{2+}]$ dynamics, relaxation and – due to its electrogenicity – potentially arrhythmogenesis in cardiomyocytes. Given NCX's central role, we set out to simulate its complex behaviour in cardiomyocyte Ca^{2+} handling with an existing mathematical model formulating the structural idea that NCX molecules are close to, but not inside, CRUs. NCX inhibition had very little effect in simulations with such a model and could not reproduce

Wilhelm Neubert studied Mathematics and Computer Science at Free University Berlin researches Numerics of Stochastic Partial Differential Equations and Cardiac Calcium Dynamics at Max Delbrück Center Berlin. **Judith Hüttemeister** Bachelor and Master of Science Degree in Biochemistry from University Jena. PhD thesis 'Sarcomere dynamics and the titin life cycle' in 2020 at the MDC (Max Delbrück Center for Molecular Medicine) and Free University Berlin. Since 2021 PostDoc at the Charité Berlin with focus on cardiac electrophysiology.

the effect of acute inhibition (Chamakuri et al., 2018; Sato et al., 2012).

In this study we formulated a model placing individual NCX molecules inside the dyadic space. We investigated the localization of NCX molecules in relation to the CRU using stimulated emission depletion (STED) super-resolution imaging in isolated ventricular rat cardiomyocytes. Model predictions were verified by spatially and temporally highly resolved Ca^{2+} imaging under control conditions and during NCX inhibition, assessing both the kinetics of stimulated Ca^{2+} transients and the occurrence and frequency of Ca^{2+} sparks.

Materials and methods

Ethical approval

All animal studies have been approved by the local ethics committee (T CH-0019/23) and were performed in accordance with the ethical standards. Animals were housed with a 12 h light/dark cycle and constant temperature in the local animal facility. They had free access to water and food. Rats were killed by decapitation under deep inhalation isoflurane anaesthesia (1.5 ml isoflurane is evaporated in an air-tight box). By testing reflexes the sufficient depth of the anaesthesia is ensured before the animal is immediately decapitated.

Isolation of adult cardiomyocytes from rats

Wild-type adult rats were used to isolate ventricular cardiomyocytes as previously described (Primessnig et al., 2016). In short, rat hearts were dissected and placed in ice cold perfusion buffer (135 NaCl, 4.7 KCl, 0.6 KH_2PO_4, 0.6 Na_2HPO_4, 1.2 $MgSO_4$, 10 HEPES, 30 taurin, 10 BDM, 10 glucose; mM). The aorta was cannulated and the heart was perfused for 2 min at 37°C with perfusion buffer before enzymatic digestion was started by switching to buffer containing Liberase TM (Sigma–Aldrich, 75 µg/ml) for 13 min. The digested heart tissue was gently pulled apart and reaction was stopped by adding buffer containing 10% BSA and 12.5 µM $CaCl_2$. After careful dispersion, cells were filtered and allowed to settle. Calcium concentration was increased stepwise to 1 mM and finally cells were resuspended in NT1 (Normal Tyrode) solution (136 NaCl, 4 KCl, 1 $MgCl_2$, 10 HEPES, 10 glucose) plus 1 $CaCl_2$ (number always corresponds to $[Ca^{2+}]$ in mM).

Fixation and staining of cardiomyocytes for STED imaging

Junctophilin-2 (JPH-2) was used as a dyadic cleft marker since it provides the physical link between the T-tubule membrane and the SR, forming and maintaining the cardiac dyad (Setterberg et al., 2021). Adult cardiomyocytes were seeded on coverslips coated with laminin and were fixed with 4% PFA for 10 min after settlement for 2 h. Cells were permeabilized (0.3% TritonX100, 10% goat serum, 0.2% BSA in PBS) for 2 h and stained with the primary antibody (anti-RyR 1:50, MA3-916 Thermo Fisher; anti-JPH 1:100, PA5-20 642 Invitrogen; anti-NCX 1:200, R3F1 swant) overnight at 4°C. After washing, cells were incubated with the secondary antibody (STAR-orange anti-rabbit and STAR-red anti-mouse, abberior) 1:200 in dilution buffer (0.025% TritonX100, 2% goat serum, 1%BSA) for 2 h at room temperature. The stained cells were washed again with dilution buffer before mounting them with solid anti-fade mounting medium (abberior).

STED super-resolution imaging and distance calculation

Imaging was done with a 3D-STED microscope (abberior Instruments GmbH, Göttingen, Germany). A confocal overview image of the whole cell was captured with a pixel size of 80 nm. For STED imaging, a region of interest (ROI) with a size of 10 × 10 μm^2 was selected and imaged with 8× line accumulation and a pixel size of 20 nm.

Prior to the analysis, images were post-processed by subtraction of median-filtered images (50 pixels) from the original with Fiji image processing software. The distance calculation between clusters of NCX and JPH or RyR and JPH, respectively, was done with the DiAna Plugin (Gilles et al., 2017). For the segmentation, the iterative filter was used with an object size from 4 to 200 pixels. The distances of the clusters were calculated centre–centre and edge–edge with inclusion of overlapping clusters by selection of the first and second closest objects. Median distances between NCX clusters and the closest JPH cluster (or RyR to JPH) and the frequency distribution of the distances were calculated per image. For NCX, 31 images were acquired from three different rat cell isolations and for RyR, 20 images from one rat.

Confocal line scan imaging

Adult cardiomyocytes were seeded on laminin-coated, glass-bottom dishes and loaded with 2 µM of the calcium-sensitive dye Fluo-4 AM (Thermo Fisher) dissolved with 0.05% Pluronic F-127 after 10 min of attachment. Stained cells were washed with NT1 buffer and placed under a confocal microscope (LSM810, Carl Zeiss). Cardiomyocytes were constantly perfused with NT buffer heated to 37°C during imaging. We performed the experiments under three different buffer conditions: NT1 buffer contains 1 mM calcium, NT5 5 mM and NT5low 5 mM calcium and only 68 mM sodium. Cardio-

myocytes are pre-stimulated at 1 Hz for 1 min while perfused with the respective buffer. Scan lines were selected longitudinally through the whole cell (512 pixels, pixel size 0.10–0.24 μm). Imaging was usually done for 30 s at maximal speed (1.24 ms/line) while cells were stimulated at 1 Hz for the first 5 s. Each cell was first recorded during perfusion with NT buffer before the NCX was inhibited with ORM-00 10564 at 1 μM for 1 min after which recording was repeated. Imaging was started again 5–10 s after restarting the electrical pacing at 1 Hz. To quantify SR calcium release and reuptake, a subset of cardiomyocytes was transfused with caffeine at 30 mM.

Calcium-dependent fluorescence intensity (F) was normalized to the diastolic fluorescence intensity directly before stimulation (F/F_{dia}) or to the diastolic fluorescence intensity before NCX inhibition (F/F_0, see also scheme in Fig. 6*D*) and a mono-exponential curve was fitted to the $[Ca^{2+}]$ decay (starting at 90%) by a custom-made algorithm as described before (Semmler et al., 2024). Calcium amplitude, TF50 (time to half-maximal $[Ca^{2+}]$ amplitude), time-to-peak and decay tau were calculated using the F/F_{dia} normalization while the total calcium peak is calculated with the F/F_0 normalization. Normalized images (F/F_{dia}) were used to segment and quantify the frequency of waves and sparks starting 1 s after the last stimulus. Statistics were performed per cell in pairwise fashion (same cell before and after treatment) with $n = 16$ for NT1, $n = 20$ for NT5 and $n = 10$ for NT5low from four animals.

Statistics

Statistical analysis was performed with GraphPad Prism 9.5.1. Results from all cells are calculated as means ± SD and depicted with individual values in scatter plot diagrams with SD as error bar. Paired data (same cell before and after treatment) are connected by a black line. Differences between two groups were tested by *t* test and between three groups by one-way ANOVA post-Tukey. Comparisons with two different parameters (treatment and buffer condition) are tested with a two-way ANOVA post-Tukey. Significance is indicated as follows: $^{*}P < 0.05$, $^{**}P < 0.01$, $^{***}P < 0.001$ and $^{****}P < 0.0001$. Exact *P* values are indicated in the figures for all results mentioned in the main body and any significant differences. For diagrams with two parameters, all exact *P* values (also the not-mentioned comparisons) can be found in the data table in the Supporting information.

In silico modelling

We use our previously published model (Chamakuri et al., 2018; Cosi et al., 2019; Neubert et al., 2026; Vierheller et al., 2015) with electrophysiological parameters for rat based on Stevenson-Cocks (2019). The detailed equations defining the model can be found in these publications. Since we simulate sparks at resting potential only, the results will not be affected by details of the electrophysiology model but rather by the Ca^{2+} concentration dynamics in the dyadic cleft, junctional SR (JSR), network SR and cytosol. The bulk Ca^{2+} concentration dynamics are modelled by a full solution of the reaction–diffusion equations for Ca^{2+} in the cytosol and network SR on sub-micrometre and millisecond scale with finite element methods. We recently added space–time adaptivity to the finite element methods which allows Ca^{2+} sinks to be included inside dyadic clefts (Neubert et al., 2026). Sub-dyadic concentration gradients during sparks cover hundreds of micrometres and consequently Ca^{2+} channel cluster structure within the dyadic cleft affects spark properties (Cosi et al., 2019; Vierheller et al., 2015). As we will see below, sub-dyadic gradients caused by NCX are also relevant at resting level concentrations. Therefore, we take this sub-dyadic detail and bulk concentration dynamics into account. The spatially resolved representation of CRUs considers individual LCC and RyR channels and their stochastic channel state transitions, RyR cluster structure according to Jayasinghe et al. and Cosi et al. (Cosi et al., 2019; Jayasinghe et al., 2018), and dynamic JSR concentration. The $[Ca^{2+}]$ gradients inside the cleft caused by channel currents and electrodiffusion are calculated with quasi-stationary Green's functions (Schendel et al., 2012; Soeller & Cannell, 1997). Preliminary simulations using the previously published model (Cosi et al., 2019; Vierheller et al., 2015) indicated that the effects of NCX outside the dyadic space on spark rate were not significant enough to create the whole cell effects observed in our earlier experiments (Primessnig et al., 2019; Primessnig et al., 2016).

Therefore, we expanded the model by including individual NCX molecules inside the dyadic space. The NCX channels are distributed on the plasma membrane or T-tubule membrane next to the LCC channels. The current for an individual NCX is computed as follows:

$$\boldsymbol{J}_{\mathrm{NCX}} = \boldsymbol{g}_{\mathrm{NCX,CRU}} \cdot \frac{\boldsymbol{K}_a \cdot \left(\boldsymbol{e}^{\eta z}\left[\boldsymbol{Na}^{+}\right]_i^3\left[\boldsymbol{Ca}^{2+}\right]_o - \boldsymbol{e}^{(\eta-1)z}\left[\boldsymbol{Na}^{+}\right]_o^3 \boldsymbol{c}_{\mathbf{di}}\right)}{(\boldsymbol{t}_1 + \boldsymbol{t}_2 + \boldsymbol{t}_3)\left(1 + \boldsymbol{K}_{\mathbf{sat}}\boldsymbol{e}^{(\eta-1)z}\right)} \quad (1)$$

$$t_1 = K_{\mathrm{mCai}}\left[Na^{+}\right]_o^3\left(1 + \left(\frac{\left[Na^{+}\right]_i}{K_{\mathrm{mNai}}}\right)^3\right) \quad (2)$$

$$t_2 = K_{\mathrm{mNao}}^3 \cdot c_{\mathrm{di}} \cdot \left(1 + \frac{c_{\mathrm{di}}}{K_{\mathrm{mCai}}}\right) \quad (3)$$

$$t_3 = K_{\mathrm{mCao}} \left[Na^+\right]_i^3 + \left[Na^+\right]_i^3 \left[Ca^{2+}\right]_o + \left[Na^+\right]_o^3 c_{\mathrm{di}} \quad (4)$$

where $g_{\mathrm{NCX,CRU}}$ is the exchange rate of a single NCX molecule, c_{di} is the Ca^{2+} concentration at the exchanger's location in the dyadic space and all other parameters are as described in Shannon et al. (2004).

Including the NCX in the CRU introduced several new challenges. The NCX is always in a conducting state (both LCCs and RyRs have resting or closed states in which they are non-conductive), its flux is nonlinear in cytosolic $[Ca^{2+}]$ (both LCC and RyR fluxes are linear in $[Ca^{2+}]_i$, while NCX exhibits biphasic behaviour, see Figs *A*2, *A*3), and NCX acts as a Ca^{2+} sink in the dyadic space during Ca^{2+} release and under certain external conditions even at rest. The first property requires that the concentrations inside the CRUs must be explicitly computed not only during release, but even at rest. This incurs a significant computational cost, especially during spark simulations. Our recent advances with locally adaptive grids (Neubert et al., 2026) are most effective in exactly these types of simulations, thus partially compensating for this loss of efficiency. We deal with the non-linearity of NCX and its nature as a Ca^{2+} sink in the CRU by using a dampened Newton's method to solve the non-linear parts of the current equations to compute intra-CRU Ca^{2+} concentrations.

Results

Localization of NCX in relation to dyadic cleft

We performed STED super-resolution imaging on intact isolated adult rat cardiomyocytes (Fig. 1) to obtain information about the exact location of NCX with regard to the dyadic cleft. We co-stained for junctophilin (JPH) as a marker for the dyadic cleft (Setterberg et al., 2021). We found that NCX localizes mainly at the T-tubuli, close to the JPH staining (Fig. 1*A*). For a comparison to a known localization in the dyadic space, we also co-stained RyR with JPH (Fig. 1*B*), which exhibits a similar pattern, but a more exclusive co-localization.

Every image channel is filtered, thresholded and segmented (Fig. A1*A*, *B*) for the distance calculation. About 300–500 NCX (or RyR) clusters were detected in every 10 × 10 µm segmented image. Centre-to-centre (scheme in 1E) and edge-to-edge (scheme in 1F) distances to the closest JPH cluster were measured. The largest fraction of NCX and RyR clusters have an edge-to-edge distance equal to zero, corresponding to overlapping with the closest JPH cluster (Fig. 1*C*, NCX: 25.8%, RyR: 30.9%) with a significant difference ($P = 0.0455$) between NCX and RyR. The percentage of NCX clusters with the closest JPH cluster more than 0.5 µm away is significantly higher ($P < 0.001$) than for the RyR cluster (5.5% *vs.* 0.7%). Although RyR clusters are a bit closer to JPH than NCX, 46.95% of the NCX cluster have still an edge-to-edge distance below the estimated resolution limit of the microscope of 50 nm (Fig. 1*D*) and 16.28% of NCX clusters have even a centre-to-centre distance under the resolution limit (Fig. A1*D*). The median distance from NCX to the closest JPH is 0.13 µm centre-to-centre (Fig. 1*E*) and 0.07 µm edge-to-edge (Fig. 1*F*) compared with 0.11 µm and 0.04 µm for the RyR–JPH distances. Most NCX and RyR are 0.05–0.1 µm centre-to-centre distance away from the closest JPH cluster (Fig. A1*C*), suggesting a localization inside or close to the dyadic cleft for most NCX, while the larger median distance can be understood as an indication that NCX also exists far from dyadic clefts as opposed to RyRs who are almost exclusively located in the dyadic cleft.

In silico modelling of calcium dynamics

As the available literature on NCX is largely concerned with its whole-cell exchange rates, we could not find individual NCX molecule recordings to estimate its exchange rate under physiological conditions. To get an estimate for the impact of individual NCX molecules and to determine parameters of NCX inside the dyadic cleft, we conducted a series of simulations in which we only varied the single molecule exchange rate. We found that in the microdomain model of CRUs at resting conditions with a Ca^{2+} concentration of about 0.1 µM, the NCX flux reduces the local concentration and thus limits the current in forward mode. Therefore, changes of the maximal exchange rate $g_{\mathrm{NCX,CRU}}$ from 0.084 µMµm^3/ms to 2.52 µMµm^3/ms did not create statistically significant variations in spark morphology or rate ($P = 0.430, 0.469, 0.100$), if all other parameters were kept constant (see below and Fig. 2). For this reason, we chose $g_{\mathrm{NCX,CRU}} = 0.84$ µMµm^3/ms = 0.84 amol/s, a value from the medium range of tested exchange rates. This is similar to the values used by Lines et al. in their detailed cleft model (Lines et al., 2006). The currents during the spark simulations with resting $[Ca^{2+}]$ and V_m are substantially smaller than $g_{\mathrm{NCX,CRU}}$ (Fig. *A*2, *A*3) and very similar to the currents obtained by Hake et al. in their detailed cleft model (Hake et al., 2012).

We also simulated different geometric configurations for the NCX molecules in the microdomain: one configuration in which the NCX molecules are interspersed in the LCC cluster and one in which the NCX molecules form a ring around the outer edge of the microdomain (compare Fig. *A*4, Fig. 2*B*). The two different configurations did not entail significant differences (Fig. 2*B*; $P = 0.430$). Unless stated otherwise, all simulation results in this study refer to simulations with the interspersed NCX molecule distribution in the CRUs and a maximal exchange rate of $g_{\mathrm{NCX,CRU}} = 0.84$ µMµm3/ms.

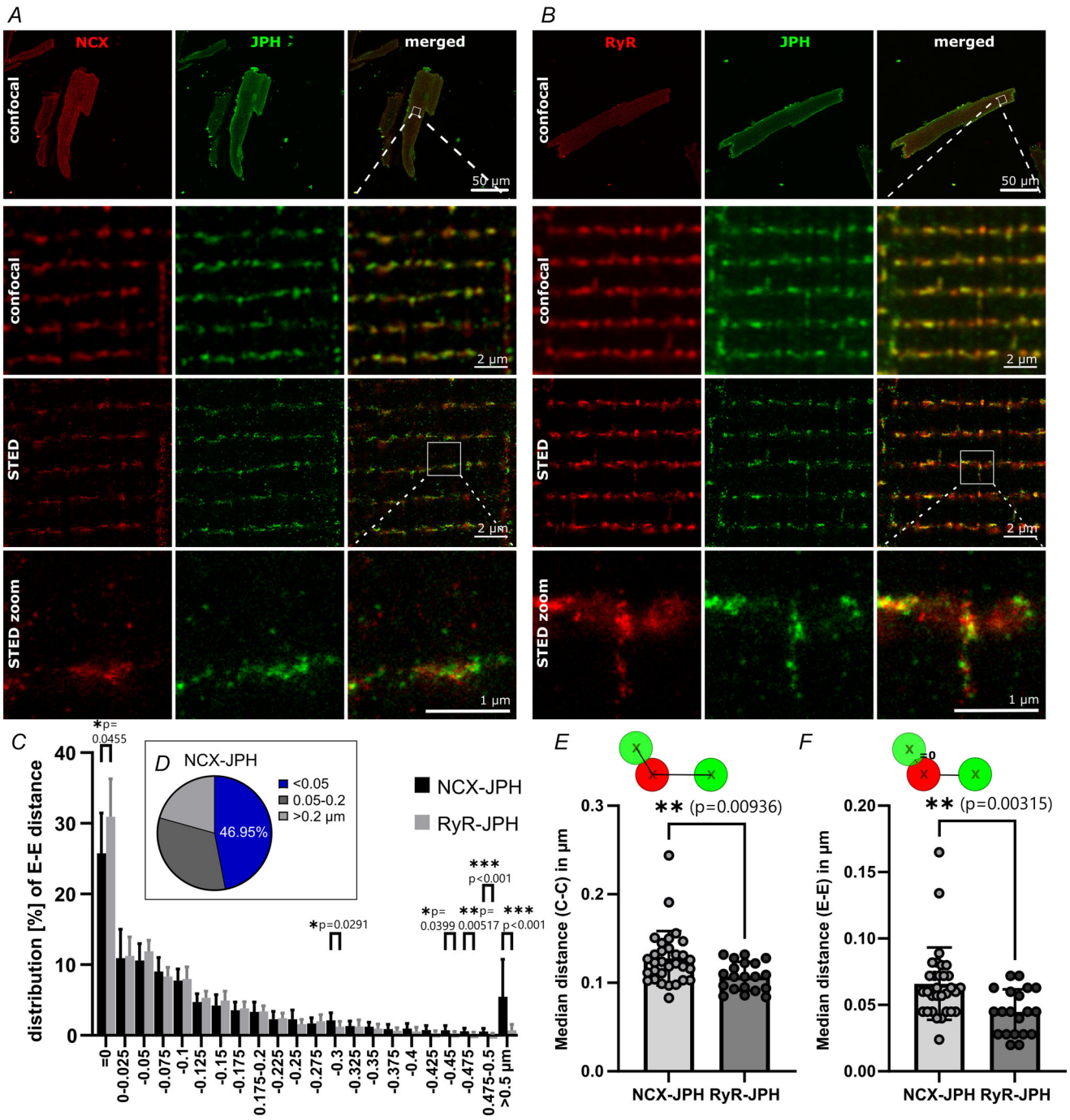

Figure 1. NCX localization relative to JPH as marker of the dyadic cleft
Immunofluorescence staining against the Na^+/Ca^{2+} exchanger (NCX) and junctophilin (JPH) (*A*) or ryanodine receptors (RyR) and JPH (*B*), respectively, was performed in adult rat cardiomyocytes. An overview image of the whole cell was done before focusing stimulated emission depletion (STED) super-resolution imaging in a 10 × 10 µm region of interest. For every STED image ($n = 31$ from three rats for NCX and $n = 24$ from one rat for RyR), the distance from every NCX cluster (or RyR, respectively) to the closest JPH cluster was determined. The histogram (*C*) depicts the distance distribution measured from edge to edge with distances = 0 indicating overlapping clusters. *D*, the percentage of NCX clusters with a distance below the resolution limit (50 nm) to the closest JPH. The median distances centre-to-centre (*E*) and edge-to-edge (*F*) were calculated per image ($n = 31$ for NCX and $n = 20$ for RyR). $^*P < 0.05$, $^{**}P < 0.01$, $^{***}P < 0.001$, tested with two-way ANOVA (*C*) or one-way ANOVA (*E*, *F*). Exact *P* values are included for significant and/or mentioned comparisons. Values for all comparisons can be found in the data table in the Supporting information.

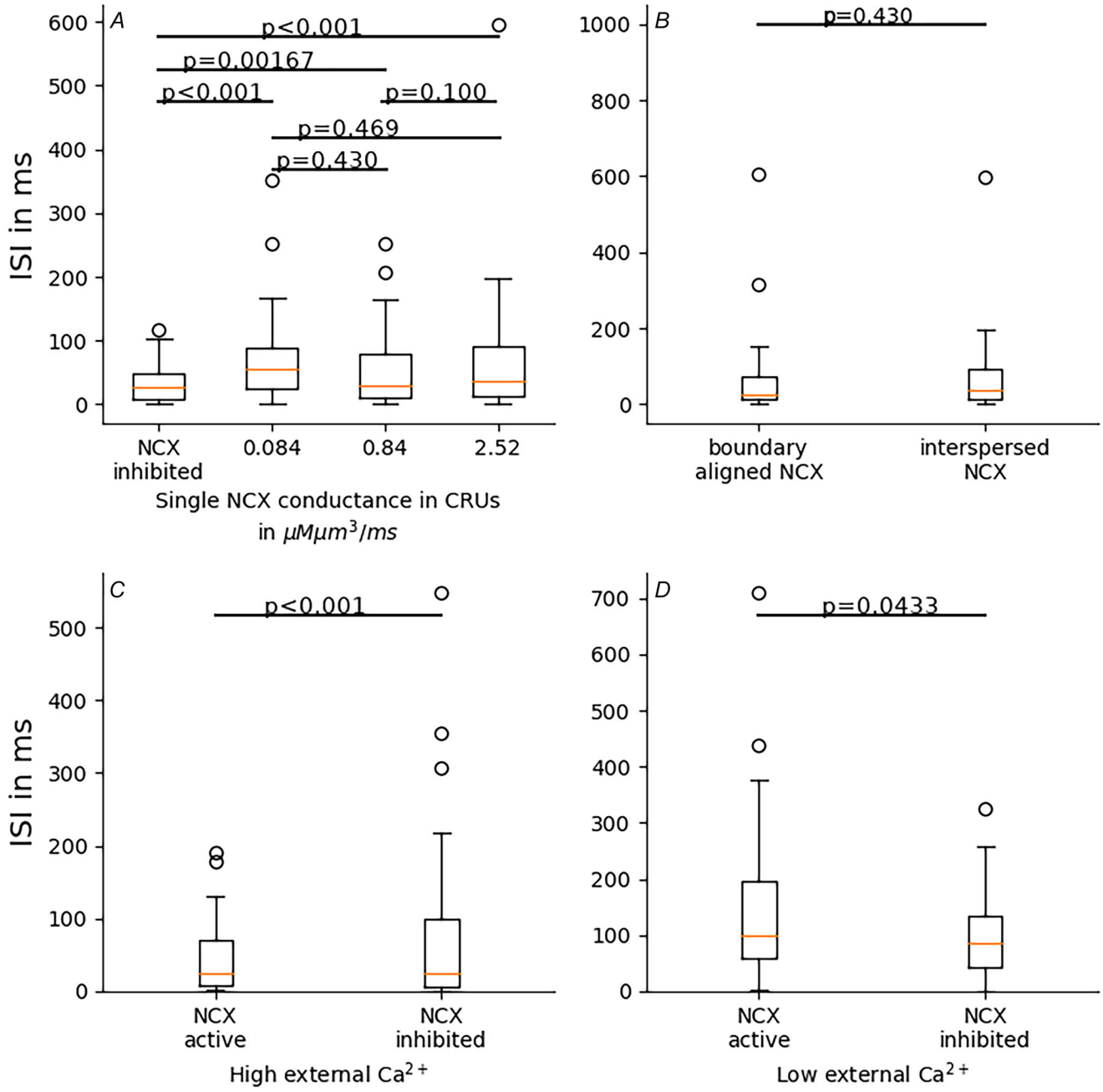

Figure 2. Simulated NCX inhibition effect on interspark intervals with different ion concentrations
All simulations were conducted with a single *z*-disc containing 396 calcium release units (CRUs) with 20 individual Na^+/Ca^{2+} exchanger (NCX) molecules per CRU and $[Na^+]_o$ = 136 mM. *A*, dependence of interspark intervals (ISIs) on maximal single NCX exchange rate at $[Ca^{2+}]_o$ = 2 mM. The leftmost column represents the state without NCX in CRUs, all n = 45. *B*, dependence of ISIs on geometric configuration of NCX locations inside the dyadic cleft. The configurations of the NCX molecules are shown in Figure *A*4, all n = 45. *C*, cells were simulated as in a buffer solution with $[Ca^{2+}]_o$ = 5 mM Ca^{2+}, resulting in NCX in reverse mode at rest. Average ISI with NCX 46.6 ms (n = 32), with NCX inhibition 81.7 ms. (n = 32). *D*, cells were simulated as in a buffer solution with $[Ca^{2+}]_o$ = 1 mM, resulting in NCX in forward mode at rest. Average ISI with NCX 146.4 ms (n = 33), with NCX inhibition 101.2 ms, (n = 33). *A–D*, the orange line shows the median. The box shows the second and third quartiles, whiskers show the range and symbols show the extreme values.

Zhang et al. showed that reducing NCX currents non-locally, that is, by removing its fraction on tubule systems or inhibition, increases resting $[Ca^{2+}]$, and thus RyR open probability and spontaneous Ca^{2+} release (Zhang, Ni, et al., 2023; Zhang, Smith, et al., 2023). The studies used compartment models which work with spatially averaged $[Ca^{2+}]$ in the individual compartments. Hence, we decided to investigate sub-dyadic gradients and consequences of NCX presence in the dyadic space but did not alter NCX bulk densities. Fig. 3 shows calculated gradients within dyadic space. NCX in forward mode causes gradients within the dyadic space in the range of a few 10 nM. They change resting level concentrations by 20−30% in the examples shown in Fig. 3. This entails larger changes in RyR open probability since this probability depends non-linearly on dyadic $[Ca^{2+}]$. Already a single open RyR causes a substantial increase of dyadic $[Ca^{2+}]$, entailing steep gradients. Some RyR close to the open one experience concentrations in the tens of micromolar range, but many RyR experience concentrations in the micromolar range. NCX currents affect these gradients in this concentration range as the difference plots show. If many RyR are open, they completely compensate NCX currents and NCX-related gradients are negligible. Consequently, simulated spark morphology (full duration at half maximum (FDHM) and peak $[Ca^{2+}]$) was not affected by the presence or absence of NCX molecules in the CRUs or their geometric distribution, regardless of external ion concentrations (see Fig. 4).

This holds true across the simulated range of maximal exchange rates and for both tested NCX array configurations. The datasets for the interspersed NCX configuration with high maximal exchange rate $g_{NCX,CRU}$ and the reduced maximal exchange rate show a statistically significant difference for both peak $[Ca^{2+}]$ and FDHM ($P = 0.0141$ and $P = 0.0460$, respectively), when compared directly with each other. All other configurations when compared with these two or each other indicate no statistically significant difference in those parameters ($P = 0.068$–0.9795, for a full list of all P values see the Appendix). We thus assume the single divergent dataset pair to be a statistical outlier.

Comparing the average interspark intervals (ISIs) between different parameter sets showed a more interesting picture. First, it should be noted that here too, the geometric distribution of NCX in the CRUs did not seem to have any impact: comparing ISIs for the interspersed distribution (65.2 ± 94.4 ms) and the boundary aligned distribution (63.7 ± 99.8 ms) showed no significant difference ($P = 0.430$), see Fig. 2*B*.

On the other hand, there were significant differences between the presence and absence of NCX molecules in the CRUs. Under physiological conditions ($[Ca^{2+}]_o = 2$ mM, $[Na^+]_i = 11$ mM, $[Na^+]_o = 136$ mM), the average ISI increased by 50% from 36.4 ± 33.1 ms without NCX in the CRU to around 60 ms with NCX, almost independent of maximal single molecule exchange rate (compare Fig. 2*A*, average ISI with NCX 52.6–65.2 ms, for $g_{NCX,CRU} = 0.84$ $P = 0.00167$, all other $P < 0.001$). However, as long as individual NCX molecules were included in the simulation and single NCX molecule exchange rate was sufficiently large, varying $g_{NCX,CRU}$ as in Fig. 2*A* did not significantly affect spark rate ($P = 0.100$–0.470, for a full list of all P values, see the Appendix).

When comparing ISIs under varied external ion concentrations, different ISI responses could be observed. We start with conditions entailing the reverse mode of the NCX corresponding to the experimental condition NT5 (see *Materials and methods* and next section). When external $[Ca^{2+}]$ was high ($[Ca^{2+}]_o = 5$ mM), ISI was 46.6 ms. Inhibiting NCX inside the CRUs increased ISI by 75% to 81.7 ms ($P < 0.001$). NCX was in reverse mode at rest at these ion concentrations (see Fig. *A*3), transporting Ca^{2+} into the cytosol and specifically the dyadic space, thus increasing dyadic $[Ca^{2+}]$ and spark rate and decreasing ISI. When NCX was inhibited, the dyadic $[Ca^{2+}]$ decreased, leading to an increased ISI and decreased spark rate.

At the opposite end, if $[Ca^{2+}]_o$ was reduced to 1 mM (experimental condition NT1), NCX was in forward mode at rest, thus decreasing $[Ca^{2+}]$ in the dyadic space and therefore the spark rate. Our model predicts that under these conditions NCX inhibition inside the CRU leads to a decrease in ISI to 55.8% (146.4–81.7 ms on average, $P = 0.0430$).

Behaviour of NCX in calcium dynamics with different extracellular Ca^{2+} and Na^+ concentrations

As suggested by our simulations with varied external ion concentrations, we quantified $[Ca^{2+}]$ dynamics in live rat cardiomyocyte experiments with the use of the specific NCX inhibitor ORM-00 10564 (1 μM) under three different buffer conditions (NT1, NT5 and NT5low). The model prediction is, that NCX works mainly in forward mode at rest in NT1, but shifts to a preference for the reverse mode at rest in NT5. This shift is even more pronounced when sodium level is reduced in NT5low.

The same cell is measured twice, without and with ORM in the respective buffer (scheme Fig. 5*A*). Representative line scan images with corresponding transients are shown in Fig. 5*B* and in Fig. A5*B* for NT5low. Arrhythmic events such as calcium sparks and waves are quantified to see if NCX has a role in preventing them. In all recorded cells, at least a few sparks appeared as depicted in the enlarged view (Fig. 5*C*). Waves did not occur in every cell, especially in NT1, but can be seen in the representative

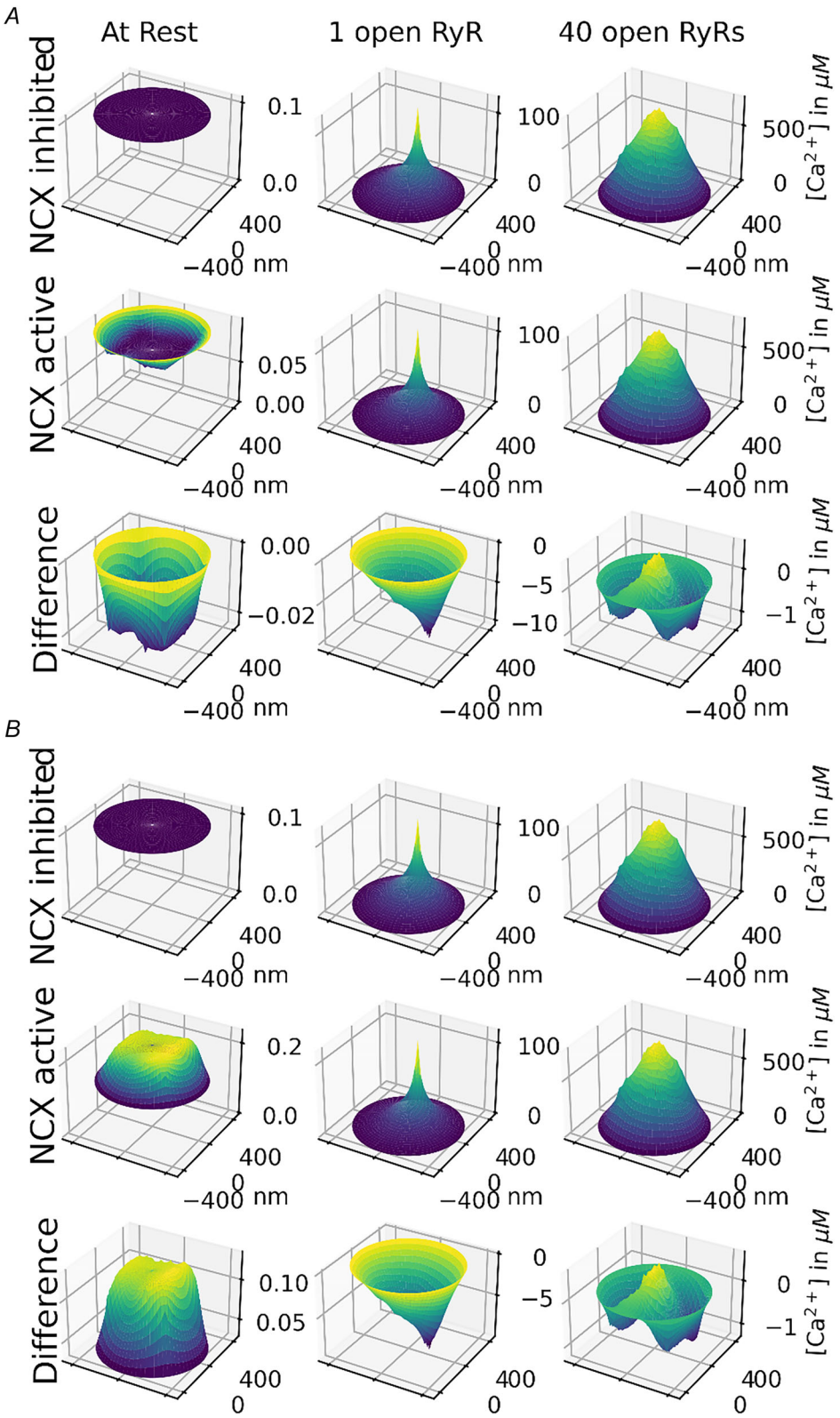

Figure 3. Sub-dyadic gradients
$[Ca^{2+}]$ concentration profiles in the dyadic cleft as seen by the ryanodine receptor (RyR) channels calculated with 20 active Na^+/Ca^{2+} exchanger (NCX) molecules in the T-tubule membrane of the cleft and 0, 1 or 40 open RyR, $[Na^+]_o$ = 136 mM, cleft radius 429 nm. The third rows in *A* and *B* show the differences in concentration caused by NCX (second row – first row). The column with one open RyR illustrates the strong gradients occurring within the cleft. *A*, NCX in forward mode with $[Ca^{2+}]_o$ = 1 mM. *B*, NCX in reverse mode with $[Ca^{2+}]_o$ = 5 mM.

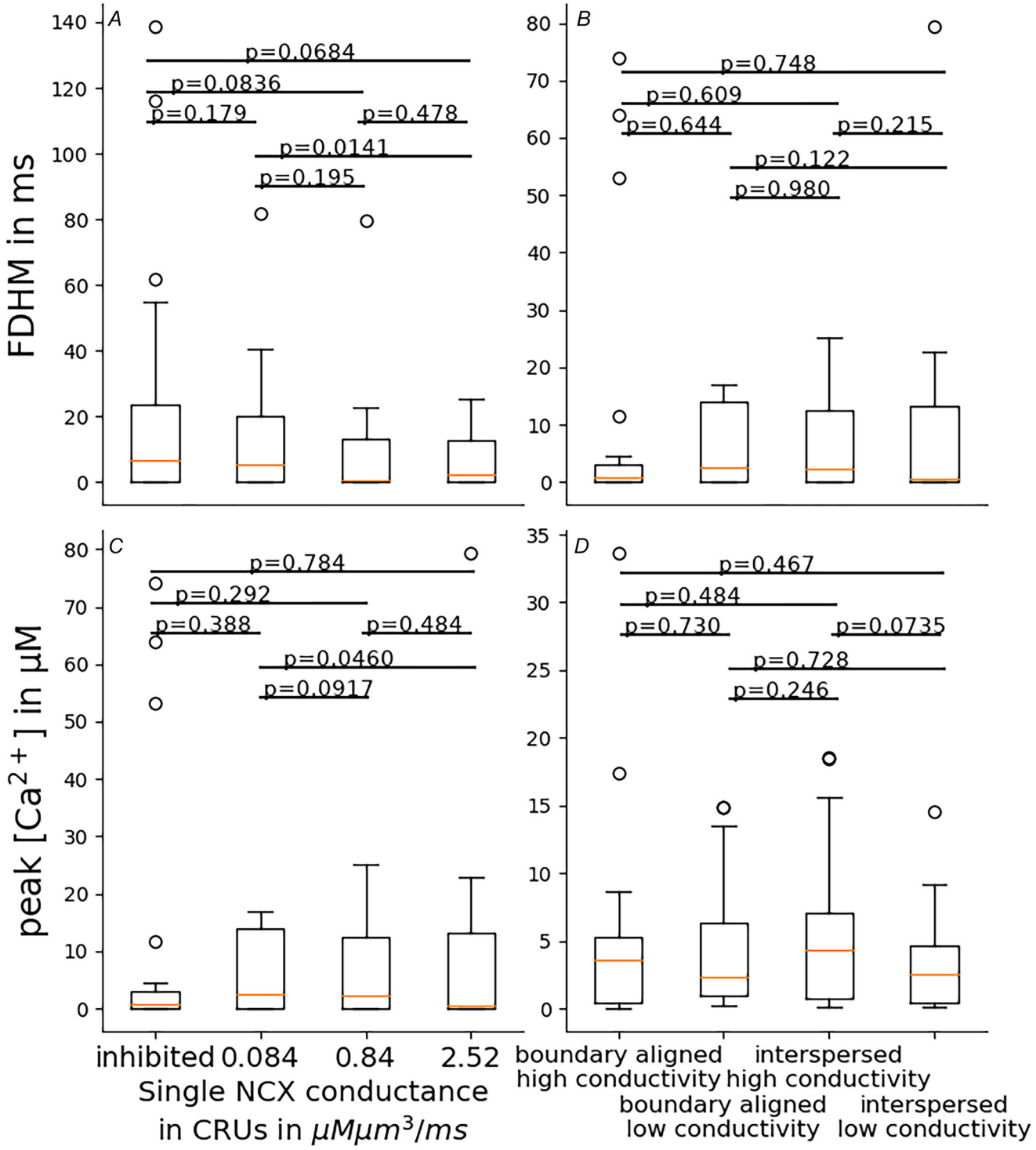

Figure 4. Impact of NCX exchange rate on spark morphology
Impact of various maximal single channel exchange rates (*A*, *C*) and geometric configurations (*B*, *D*) on full duration at half maximum (FDHM) (*A*, *B*) and peak [Ca^{2+}] during a spark (*C*, *D*) in simulations. All simulations were conducted with a single *z*-disc containing 396 calcium release units (CRUs) with 20 individual NCX molecules per CRU. There were no statistically significant differences in FDHM or peak Ca^{2+} independent of single channel maximal exchange rate or geometric configuration. *A*, *C*, all $n = 71$. *B*, *D*, all $n = 23$. *A*–*D*, the orange lines show the median. The box shows the second and third quartiles, whiskers show the range and symbols show the extreme values. Individual data points are shown if $n < 30$.

image of NT5 (Fig.5*B*, lower panel). The number of waves per second increased with higher $[Ca^{2+}]_o$ and was significantly increased ($P = 0.0321$, 0.0160 and 0.00340) with NCX inhibition in all buffer conditions (NT1, NT5 and NT5low, Fig. 5*D*). Remarkably, NCX inhibition increased spark rate only in NT1 buffer (from 1.6 ± 1.9 to 3.1 ± 3.2 sparks/s/100 µm; $P = 0.00398$), but decreased spark rate in NT5 buffer (from 3.6 ± 2.5 to 1.9 ± 1.5 sparks/s/100 µm; $P < 0.001$; Fig. 5*E*) in agreement with the simulation results (Fig. 2*C*, *D*). Control experiments with a subset of cells where no ORM was added before the second imaging, confirmed that the decrease in spark frequency under NT5 is indeed caused by NCX inhibition ($P = 0.0040$) and not just by a temporal effect (control $P = 0.602$; Fig. A2*G*).

Since NCX had an effect on spark rate, we also investigated cytosolic $[Ca^{2+}]$ dynamics during action potentials with and without NCX inhibition. Representative images of calcium transients during electrical field stimulation are shown in Fig. 6*B*–*C* (for NT1 and NT5). The $[Ca^{2+}]$ amplitude (F/F_{dia}) is a measure of RyR-mediated Ca^{2+} release since it is normalized to F_{dia} directly at the beginning of the respective stimulation. F/F_{dia} remained unchanged in NT1 during NCX inhibition ($P = 0.966$) but declined significantly in high $[Ca^{2+}]_o$ ($P < 0.0001$; Fig. 6*F*). However, since there was a significant increase in diastolic $[Ca^{2+}]$ by inhibition of NCX in all buffer conditions (Fig. 6*E*; $P = 0.00890$, $P < 0.001$, $P = 0.00468$), we also normalized to the diastolic fluorescence intensity (F_0) before the inhibition (Scheme Fig. 6*D*). The peak value (F/F_0), representing available calcium for contraction, increased in NT1 ($P = 0.0334$) and mildly decreased in NT5 ($P = 0.0331$) when NCX was inhibited

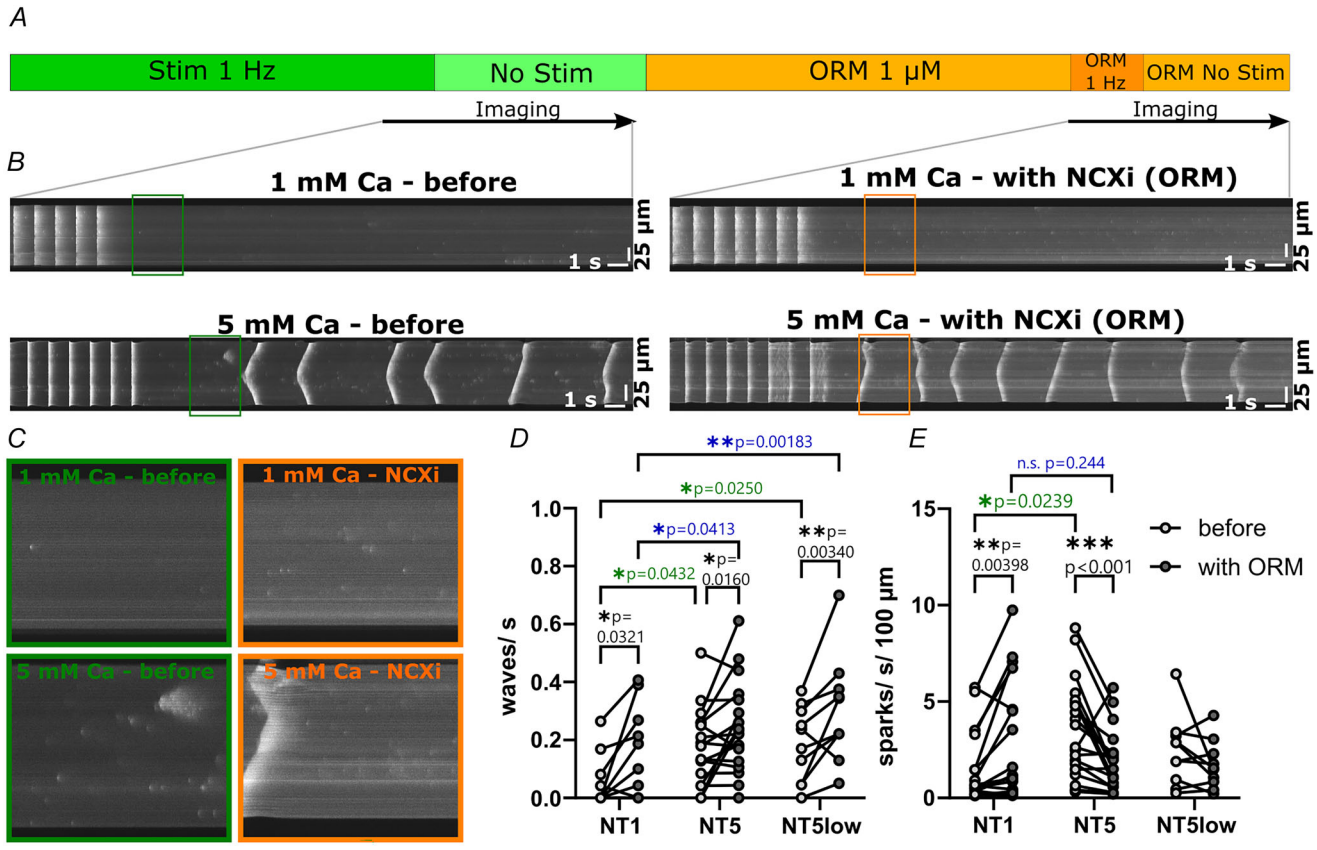

Figure 5. NCX-dependent arrhythmic events
Recording of $[Ca^{2+}]$ transients was started after 1 min of pre-stimulation and consisted of a short period (5 s) of 1 Hz steady-state stimulation followed by a period without stimulation (*A*, *B*) to record waves and sparks. Whole recording (*B*) and short zoom (*C*) were used to depict waves and sparks better. The incidence of waves (*D*) increased with extracellular calcium concentration and during Na^+/Ca^{2+} exchanger (NCX) inhibition. Sparks are quantified per second and 100 µm (*E*) and the inhibition of NCX causes an increase of spark rate at normal $[Ca^{2+}]_o$ (NT1), but a decrease in high $[Ca^{2+}]_o$ (NT5). $^*P < 0.05$, $^{**}P < 0.01$, $^{***}P < 0.001$, tested with paired two-way ANOVA per cell ($n = 16$ for NT1, $n = 20$ for NT5 and $n = 10$ for NT5low with four animals). Black asterisks (*) indicate differences between before and with ORM, green asterisks between different $[Ca^{2+}]_o$ without and blue asterisks with ORM treatment. Exact *P* values are included for significant and/or mentioned comparisons. Values for all comparisons can be found in the data table in the Supporting information.

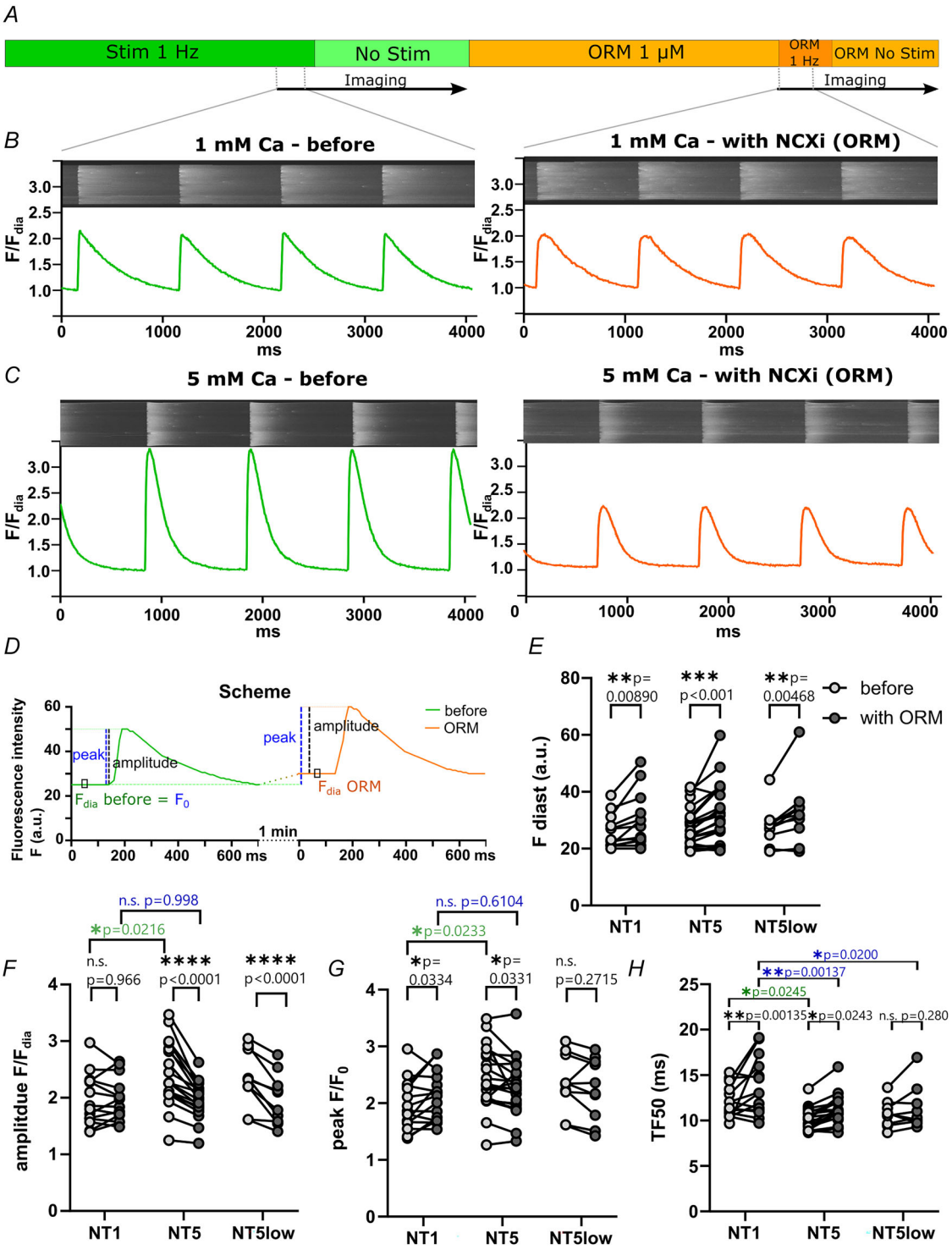

Figure 6. NCX-dependent calcium handling
Adult rat cardiomyocytes were loaded with the Ca^{2+}-sensitive dye Fluo4-AM. Cells are stimulated at 1 Hz for 60 s and [Ca^{2+}] transients were quantified with confocal line scan imaging for 30 s (first 5 s with stimulation, *A*). After superfusion with 1 µM ORM (Na^+/Ca^{2+} exchanger (NCX) inhibitor) the measurement was repeated in the same cell. *B*, representative [Ca^{2+}] transient before and during ORM treatment in 1 mM calcium solution (NT1) and 5 mM calcium solution (NT5) as fluorescence intensity normalized to diastolic values at the start of stimulation (F/F_{dia}) (*C*). The scheme (*D*) depicts how the absolute calcium-dependent fluorescence intensity was normalized to the diastolic value immediately before the stimulation for most measurements (F_{dia}, *E*) with the amplitude as

maximal value (*F*). However, due to the increase in diastolic calcium (*E*), we also normalized $[Ca^{2+}]$-dependent fluorescence to the diastolic value before NCX inhibition (F_0) with the peak as maximal value (*G*). Not only diastolic and peak $[Ca^{2+}]$ were affected by NCX inhibition, but also the time to half-maximal $[Ca^{2+}]$ amplitude (TF50) increases (*H*). $^*P < 0.05$, $^{**}P < 0.01$, $^{***}P < 0.001$, $^{****}P < 0.0001$ per cell ($n = 16$ for NT1, $n = 20$ for NT5 and $n = 10$ for NT5low with four animals), tested with paired two-way ANOVA. Black asterisks indicate differences between before and with ORM, green asterisks between different buffers before ORM and blue asterisks between different buffers with ORM treatment. Exact *P* values are included for significant and/or mentioned comparisons. Values for all comparisons can be found in the data table of the Supporting information. NT5low buffer contains 5 mM calcium and reduced sodium (68 mM).

(Fig. 6*G*). Both amplitude ($P = 0.0216$) and peak $[Ca^{2+}]$ ($P = 0.0233$) were increased in high $[Ca^{2+}]_o$ as compared with NT1, but this difference was abolished after NCX inhibition ($P = 0.998$, $P = 0.6104$).

Early ('dyadic') calcium release, quantified as time to half-maximal amplitude (TF_{50}, Fig. 6*H*), was faster with NT5 *versus* NT1 ($P = 0.0245$). TF_{50} was slowed after NCX inhibition in both NT1 and NT5 ($P = 0.00135$, $P = 0.0243$). Similarly, time-to-peak $[Ca^{2+}]_i$ (TTP) was slowed with NCX inhibition (Fig. A5*C*) in NT1 ($P < 0.0001$), but not significantly prolonged in NT5 ($P = 0.0816$). In NT5low TTP was significantly higher than in NT1 and NT5 ($P = 0.0122$, 0.0294) without an additional effect of NCX inhibition ($P = 0.1393$). Calcium decay (time constant tau, Fig. A5*D*) was accelerated by NCX inhibition in NT1 and NT5low ($P = 0.0143$, 0.0111), suggesting a faster relaxation.

To prove the efficiency of NCX inhibition, a subset of cells was treated with caffeine (Fig. A5*E*) directly after stimulation. Since caffeine opens RyRs, this renders SERCA function futile and makes forward mode NCX the main mediator of calcium decay. As expected, the time constant of calcium decay under caffeine was significantly prolonged with NCX inhibition (Fig. A5*F*; $P = 0.00349$).

Discussion

In this study we provide direct evidence in intact cardiomyocytes that NCX molecules localize within the dyadic cleft and thereby directly modulate local Ca^{2+} dynamics. By combining super-resolution imaging, computational modelling, and functional measurements we show that dyadic NCX bidirectionally regulates spark activity and contributes to the early phase of Ca^{2+} transients in a mode-dependent manner. These findings uncover a previously underappreciated role of NCX in shaping both spontaneous and evoked Ca^{2+} release, providing a mechanistic basis for its paradoxical effects under different extracellular conditions.

NCX has a central role in the Ca^{2+} cycle in cardiomyocytes as underpinned by a large body of research on the subject. The exact position of the NCX with regard to cleft space is a matter of discussion which is based on data on immunofluorescence localization, NCX co-localization with RyR and LCC, NCX density in T-tubule membrane and current measurements (see Aronsen et al. and Langer & Peskoff for reviews (Aronsen et al., 2013; Langer & Peskoff, 1997)). It is worthwhile looking at the use of language in this context. The review by Langer and Peskoff talks about LCCs and RyRs as within the cleft space. At the same time, the authors describe NCX location as at the cleft spaces (Langer & Peskoff, 1997). Modelling studies reflect this discussion, too. Some compartment models place NCX at the dyadic space (Colman, 2019; Conesa et al., 2020; Higgins et al., 2007; Shiferaw et al., 2020; Shiferaw et al., 2017), while others put it (additionally) within it (Lines et al., 2006; Zhang, Ni, et al., 2023; Zhang, Smith, et al., 2023). Sher et al. as well as Sato and Bers investigated both choices (Sato et al., 2012; Sher et al., 2008). Some spatially detailed models of dyadic space used NCX inside the dyadic cleft (Hake et al., 2012; Lines et al., 2006) while others do not (Cannell et al., 2013; Sheard et al., 2019; Stern et al., 1999; Walker et al., 2014). The variety of studies focusses on different aspects among which the role of the NCX reverse mode for CICR triggering during depolarization has a prominent role. A general conclusion which can be drawn is that the effect of NCX on dyadic $[Ca^{2+}]$ and RyR open probability is substantially stronger if NCXs are within the cleft rather than at the cleft. Beyond reaffirming junctional enrichment, our combined structural–functional–computational data provide direct evidence that dyadic localization is not merely compatible with, but functionally required to explain the direction and magnitude of NCX effects on local Ca^{2+} release in intact cardiomyocytes.

Using super-resolution imaging we demonstrated that NCX and RyR clusters can both be found in close proximity to JPH. Almost half of all NCX clusters were closer to JPH than the estimated resolution limit (50 nm, Fig. 1*D*), with 25.8% of NCX clusters even overlapping directly with JPH clusters (Fig. 1*C*). A similar amount of co-localization (27%) was reported directly between NCX and RyR (Jayasinghe et al., 2009). Some NCX clusters were far from any JPH (5.5% distance >0.5 μm), which was much less the case for RyRs (0.7%, Fig. 1*C*). NCX median edge-to-edge distance to the closest JPH cluster was around 70 nm, compared with 40 nm for the RyR clusters (Fig. 1*F*). This might simply illustrate that NCX

may be located inside as well as next to dyadic clefts which is unlikely for RyRs. The average distance for both molecules was much smaller than the diameter of the dyadic SR junction of about 250–650 nm (Brochet et al., 2005) as well as the diameter of a typical RyR cluster in a CRU, which can reach hundreds of nanometres (Jayasinghe et al., 2018). Therefore, our data provide strong evidence for NCX molecules located within the CRU.

STED imaging is at its core a 2D projection of a complex 3D geometry, involving several membranes closely wrapped around each other. Compared with conventional confocal microscopy, the 2D-STED configuration reduces partial-volume effects mainly through improved lateral resolution. Applying the STED laser also at the *Z* axis (3D STED) is possible, but challenging since it causes increased photobleaching and a lower resolution (and signal to noise) in the XY plane with less robust cluster segmentation. Therefore, we focused on 2D STED imaging with the limitations it may cause in interpreting complex 3D structures. A moderate residual axial partial-volume effect may cause some apparent co-localization in 2D to reflect axial averaging rather than true overlap, but this primarily affects precise spatial assignment and does not change conclusions about close proximity and functional relevance. The proximity of the clusters is highly suggestive of a closer relationship between NCX and RyR clusters but is by itself not enough to demonstrate involvement of NCX in regulating $[Ca^{2+}]$ within the CRU. Functional verification was required.

When the cell is at rest and a cluster is not currently participating in a spark or wave, the resting $[Ca^{2+}]$ in the cluster is below 0.1 μM. We hypothesized that in that range, NCX can be in either forward or reverse mode, largely depending on extracellular ion concentrations. If $[Ca^{2+}]_o$ is at 5 mM (or higher), NCX operates predominantly in reverse mode, increasing Ca^{2+} influx into the cell and the dyadic space, thus increasing the open probability of the RyRs in the local cluster. At 1 mM $[Ca^{2+}]_o$, NCX acts mainly in forward mode, promoting Ca^{2+} extrusion and thus decreasing the RyR open probability in the local cluster. Inhibiting NCX should reverse the effect in both cases. This is the behaviour exhibited by our model: inhibiting NCX in the CRUs in the high calcium simulation led to a decreased spark rate (ISI increased by 75% from 46.6 ms to 81.7 ms on average) (See Fig. 2*C*). This is in accordance with the measurements from the spark imaging experiments (Fig. 5*E*). When the cells were incubated in NT5 buffer solution (5 mM $[Ca^{2+}]_o$), administration of ORM led to a significant decrease by 47% in spark rate from 3.6 to 1.9 sparks/s/100 μm (compare Fig. 5*E*). While the numbers are quantitatively not comparable due to the different nature of the recording (the simulations measure all sparks in a single *z*-disc, while the experimental recordings measure all sparks along a longitudinal line through an entire cell), the findings are qualitatively in agreement. Modelling and observations are also consistent in low $[Ca^{2+}]_o$ conditions. NCX inhibition by ORM in NT1 led to an increased spark rate and decreased ISI both in experiments and simulations (Fig. 5*E*, Fig. 2*D*).

Interestingly, wave frequency was not reduced by NCX inhibition in NT5 buffer in our experimental data (Fig. 5*D*). Two factors play a role in wave generation: the initial spark formation and the probability to initiate more sparks (i.e. to propagate). We speculate that while sparks were simultaneously decreased under NCX inhibition at high calcium conditions in our experiments and simulations, alterations in Ca^{2+} propagation and CRU heterogeneity may contribute to the increase in wave formation. A heterogeneity of CRUs has been described (Maltsev et al., 2024) and also intracellular spots where waves preferentially start when $[Ca^{2+}]$ is high (Nivala et al., 2013), which might be more resistant to NCX inhibition. Secondly, the propagation from the initial spark to a wave might be easier with NCX inhibition due to an increased SR loading by the elevated diastolic $[Ca^{2+}]$, which makes triggering of the next CRU easier. Also, as suggested by (Bers & Shannon, 2013), some junctions may be better diffusional connected, allowing intra-SR $[Ca^{2+}]$ to sustain release above the termination threshold. Even if spark frequency is reduced and, as in our simulations average spark duration is unchanged by NCX inhibition, wave initiation may still rise due to effects on these specific JSR sites with distinct anatomical properties even when most sparks remain short and non-propagating.

Besides sparks and waves under resting conditions, we also analysed the role of NCX located at the dyad for action potential-triggered Ca^{2+} release. The rapid fluctuations of $[Ca^{2+}]$ within the dyadic cleft during an action potential lead to an even more complex regulation of NCX. There is an increase of cytosolic $[Ca^{2+}]$ at rest (diastolic $[Ca^{2+}]$) with NCX inhibition independent of external $[Ca^{2+}]$ (Fig. 6*E*), likely due to the role of NCX in Ca^{2+} export in the $[Ca^{2+}]$ decay phase. At lower external $[Ca^{2+}]$ (NT1), the $[Ca^{2+}]$ amplitude (relative increase, mostly due to SR Ca^{2+} release via RyR) is not affected by NCX inhibition (Fig. 6*F*), which leads to an increase of absolute $[Ca^{2+}]$ (peak) (Fig. 6*G*) due to the increase in diastolic $[Ca^{2+}]$. Therefore, more Ca^{2+} is available within the cell upon NCX inhibition. At elevated external $[Ca^{2+}]$ this is different, as we observed a decrease of the $[Ca^{2+}]$ amplitude upon NCX inhibition, attenuating the $[Ca^{2+}]$ amplitude increase related to increased external $[Ca^{2+}]$ (Fig. 6*F*). This suggests increased NCX reverse mode activity with higher cellular $[Ca^{2+}]$ in these electrically stimulated cardiomyocytes.

Interestingly, there was an increase in TF50 with NCX inhibition at high and low $[Ca^{2+}]_o$ (Fig. 6*H*). TF50 corresponds to the early ('dyadic') phase of Ca^{2+} release

(Heinzel et al., 2002). It has been suggested that the NCX acts in reverse mode and is thereby helping to trigger the CICR during the very early phase of activation (Larbig et al., 2010; Lines et al., 2006). Increased TF50 and thus slowed early Ca^{2+} release in experimental data support contribution of NCX in reverse mode to Ca^{2+} release at an early stage of the cardiac cycle.

Supra-physiological extracellular Ca^{2+} ($\approx$ 4–5 mM) is commonly used as a controlled Ca^{2+}-overload perturbation in isolated cardiomyocytes to promote spontaneous Ca^{2+} waves/sparks (Ferrier et al., 2003; Ford et al., 2017; Subramanian et al., 2001; Zhao et al., 2013). Here, 5 mM $[Ca^{2+}]_o$ was therefore used as a convenient probe condition to robustly bias NCX toward reverse mode, while acknowledging that such sustained levels likely exceed the reported (patho-)physiological range. Importantly, reverse-mode NCX does not require 5 mM $[Ca^{2+}]_o$, because exchanger direction is governed by membrane potential and the transmembrane Na^+/Ca^{2+} gradients and can be shifted toward Ca^{2+} influx by depolarization and/or altered Na^+ gradients (e.g. elevated $[Na^+]_i$, (Ford et al., 2017), or reduced $[Na^+]_o$, (Li et al., 2007)). In addition, restricted diffusion within the T-tubular lumen can permit transient local deviations from bulk extracellular ion concentrations (including Ca^{2+} and potentially Na^+), which may further modulate NCX driving forces during activity (Moench & Lopatin, 2014; Shepherd & McDonough, 1998; Vermij et al., 2019).

Given the agreement of theoretical model predictions and experimental data, it appears that NCX molecules are both geometrically and functionally part of the dyadic cleft. It should be investigated whether these findings extend to other species. Further, the role of the electrogenic NCX localized in the dyadic cleft on the membrane potential, specifically during repolarization, should be further studied in light of these findings. If NCX has a direct impact on (potentially arrhythmogenic) sparks during diastole, this might lead to a re-evaluation of the role of NCX for arrhythmogenic events.

Dyadic remodelling in hypertrophy and heart failure is associated with impaired ECC and contractile performance by disrupting local coupling geometry between L-type Ca^{2+} entry and RyR-dependent SR release (Gomez et al., 1997). Subcellular positioning of NCX may be relevant in this context as changes in dyadic composition and geometry could shift the local gradients 'sensed' by NCX, its mode balance, and thereby Ca^{2+} transient kinetics and mechanical performance (Gaughan et al., 1999; Ottolia et al., 2013). As inward NCX current provides a mechanistic link between spontaneous Ca^{2+} release and triggered activity, dyad-level microdomain remodelling could also modulate arrhythmia susceptibility (Landstrom et al., 2017).

Reverse-mode NCX has been implicated in multiple disease contexts and cell types. In failing and hypertrophied myocardium, altered NCX activity can modulate action potential configuration and Ca^{2+} homeostasis, potentially providing inotropic support via reverse-mode Ca^{2+} entry while also affecting electrical stability (Armoundas et al., 2003; Barry, 2000). Reverse-mode NCX has further been linked to cardioprotection in preconditioning paradigms (Li et al., 2007) to sino-atrial node pacemaking under Na^+ loading/digitalis-like conditions (Toth et al., 2022), and even to Ca^{2+} entry supporting venous contraction in vascular smooth muscle (Tykocki et al., 2012). In HFpEF models, targeting NCX entry/reverse-mode has also been explored as a strategy to improve diastolic dysfunction and remodelling (Kamimura et al., 2012; Primessnig et al., 2019; Primessnig et al., 2016).

Overall, it seems plausible and should be further explored that cardiac remodelling could modify NCX microdomain positioning and thereby influence the coupling between Ca^{2+} handling, contractility and electrical stability.

Appendix

Additional information on simulations

Beside the differences mentioned here and the parameter values mentioned in the main manuscript, all parameter values of the Ca^{2+} dynamics are as in Cosi et al. (2019) and Neubert et al. (2026). The electrophysiology parameter values are the same as in Neubert et al. (2026). We slightly adapted the parameters as shown in Table A1 to keep resting level Ca^{2+} concentration constant despite varying $[Ca^{2+}]_o$. Resting conditions are potential $V_m = -83$ mV, cytosolic $[Ca^{2+}] = 0.1$ µM, SR $[Ca^{2+}] = 1483$ µM.

Table A1. Parameter adjustments to compensate changes of resting concentrations by varying $[Ca^{2+}]_o$.

Parameter	Adjusted value with $[Ca^{2+}]_o = 1$ mM	Default value with $[Ca^{2+}]_o = 2$ mM	Adjusted value with $[Ca^{2+}]_o = 5$ mM
SERCA V^p_{max}	0.99 µM/ms	1.0 µM/ms	1.01 µM/ms
Leak flux rate g_{leak}	0.222/s	0.225/s	0.227/s
$[Ca^{2+}]_{SR}$	1483.0 µM	1200.0 µM	1483.0 µM

Na^+ cleft concentration is identical to bulk concentration, which is fixed at 11 mM and spatially homogeneous. $[Na^+]_i$ changes typically on a timescale of many seconds. In order to obtain stationary spark rates without long transients, we set intracellular $[Na^+]_i$ to the constant value of 11 mM. The NCX Na^+ ion current is three times the Ca^{2+} current. The Na^+ diffusion coefficient is equal to or larger than the free Ca^{2+} diffusion coefficient. Hence, Na^+ gradients in the dyadic space caused by NCX are larger than free Ca^{2+} gradients but smaller than three times the free Ca^{2+} gradients (see Bentele et al. for details (Bentele & Falcke, 2007). The crucial difference from Ca^{2+} is that intracellular $[Na^+]$ is in the 10 mM range. The relative change of $[Na^+]$ on that 10-millimolar level by gradients is in the order of 10^{-4} and therefore negligible. However, simulations including Na^+ diffusion are much more computationally expensive. Therefore, we decided to not include Na^+ diffusion in our simulations.

Simulations take about 2 weeks per 1 s real time simulated. Due to this long computation time for these simulations, ISI data sets for this publication are generated by several simulations with identical parameter values. They have been carried out on three 64 core AMD Ryzen Threadripper PRO 5995WX CPUs running at 4.5GHz with 256 GB of available RAM.

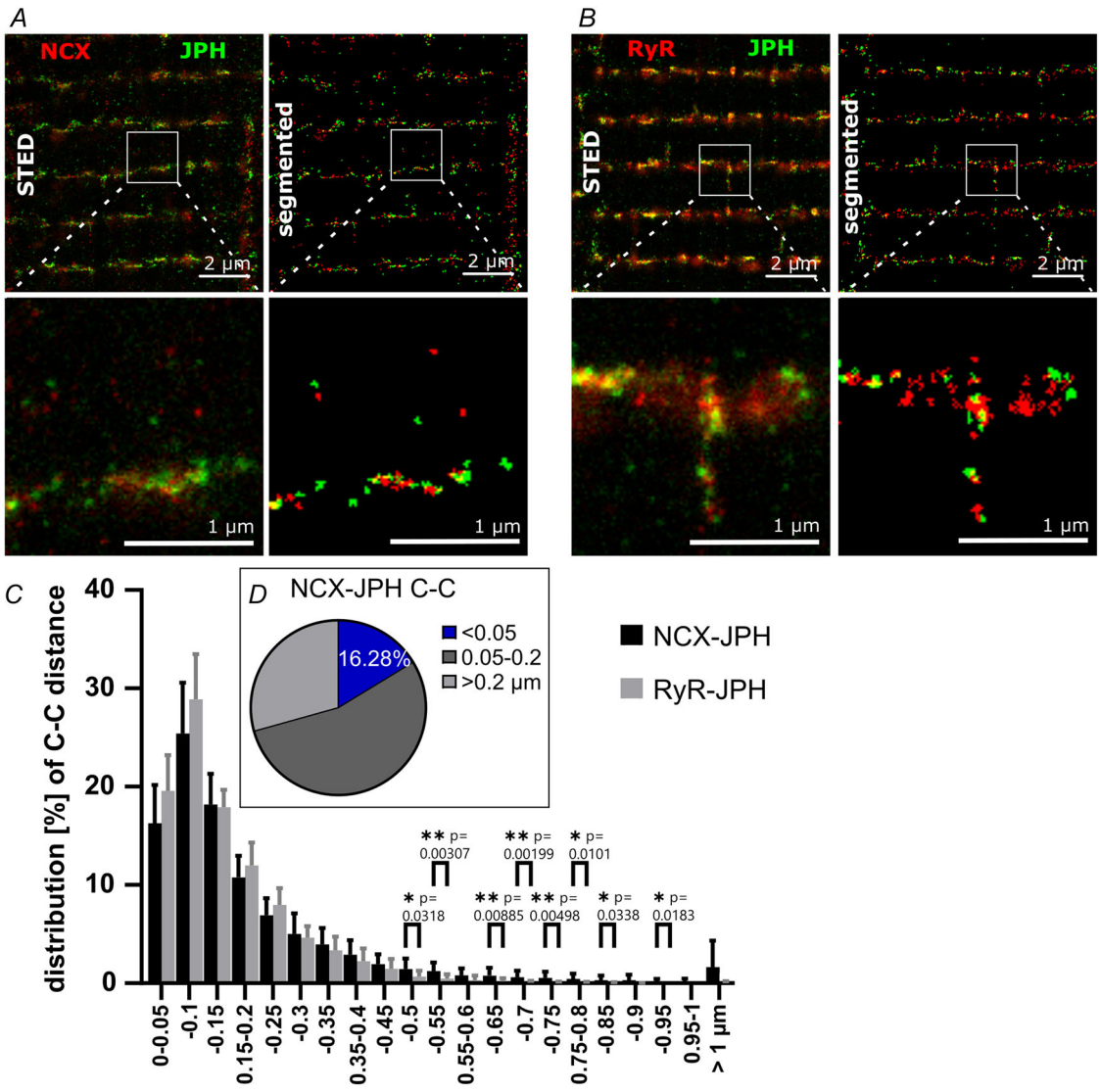

Figure A1. NCX localization
Representative segmentation as basis of the DiAna plugin for distance calculation for NCX-JPH (*A*) and RyR-JPH (*B*). Histogram with distribution of distances measured centre-to-centre (*C*). 16.28% of all NCX cluster have a centre-to-centre distance under the resolution limit (*D*). $^*P < 0.05$, $^{**}P < 0.01$, $^{***}P < 0.001$ ($n = 31$ for NCX and $n = 20$ for RyR), tested with two-way ANOVA.

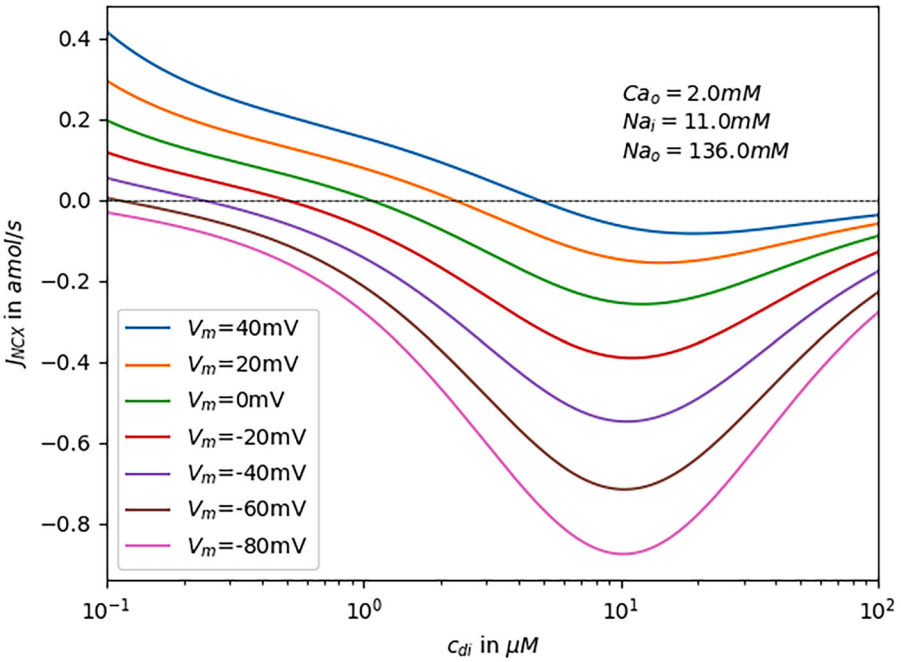

Figure A2. Biphasic dependency of NCX on dyadic [Ca^{2+}]
Na^+/Ca^{2+} exchanger (NCX) single molecule calcium current in dependence on the calcium concentration in the dyadic space according to the equations for J_{NCX} provided in section *Material and Methods*. c_{di} denotes dyadic [Ca^{2+}]. Positive calcium current values correspond to NCX operating in reverse mode. Due to the high local Ca^{2+} concentrations in the dyadic space during release events, NCX channels in the CRU will occasionally experience concentrations in the hundreds of micromolar. This means that, especially at resting membrane potentials, the biphasic nature of the effective Ca^{2+} release has to be accounted for.

The complete implementation of the space–time adaptive framework for calcium dynamics has been developed using the open-source numerical libraries DUNE (Distributed and Unified Numerics Environment) and Dune-PDELab. In our in-house code, we have implemented a specialized compile-time sparse matrix structure designed to efficiently solve large systems of partial differential equations. As a result, this customized module is not compatible with or included in the publicly released versions of Dune-PDELab. Due to licensing restrictions associated with Dune-PDELab, we are currently unable to release our modified version publicly. However, we are happy to share the complete implementation, including the source code, configuration files and detailed installation instructions, with interested researchers upon request to M. Falcke or N. Chamakuri.

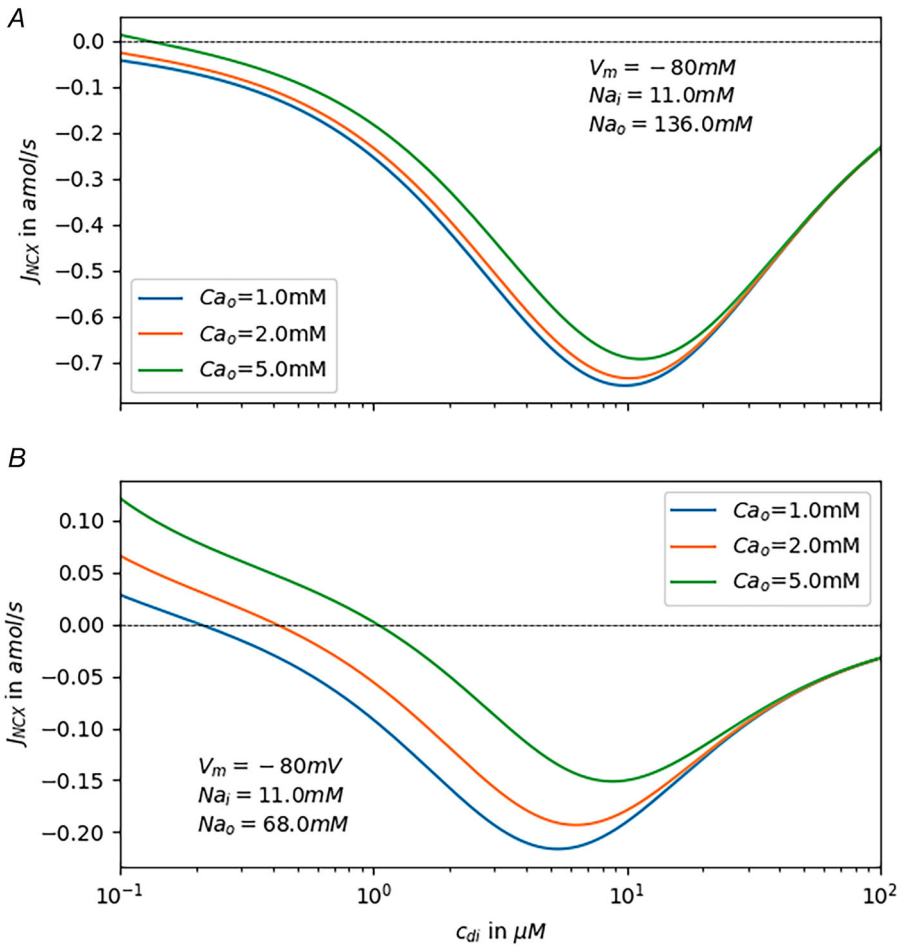

Figure A3. Dependence of NCX on extracellular Ca^{2+} concentration
Na^+/Ca^{2+} exchanger (NCX) single-molecule calcium current according to the equations for J_{NCX} provided in section *Material and Methods*. c_{di} denotes diadic $[Ca^{2+}]$. *A*, 136 mM extracellular Na^+. *B*, 68 mM extracellular Na^+. With high extracellular Na^+ and at low cytosolic Ca^{2+} concentrations, external Ca^{2+} concentration strongly impacts NCX dynamics. At 1 mM extracellular Ca^{2+} the channel is in forward mode, extruding Ca^{2+} from the cell. At 5 mM extracellular Ca^{2+} the channel is instead in reverse mode. At large cytosolic $[Ca^{2+}]$ ($\geq$ 10 µM) concentrations, the differences vanish.

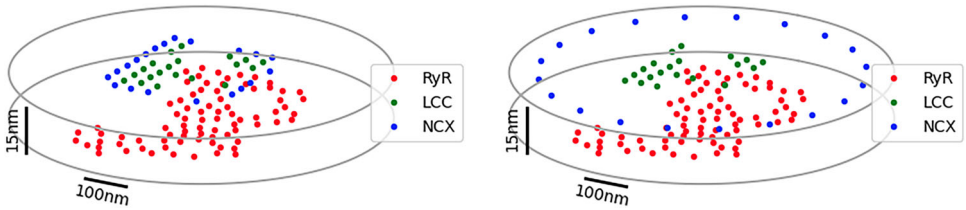

Figure A4. Two variants of NCX molecule distribution inside the dyadic space
In both panels the sarcoplasmic reticulum (SR) membrane is on the bottom and the T-tubule membrane is on top. The left panel shows the interspersed distribution, where Na^+/Ca^{2+} exchanger (NCX) is surrounding the L-type Ca^{2+} channels (LCCs) but is closer to the centre of the calcium release units (CRUs). The right panel shows the boundary-aligned distribution, in which the NCX molecules are positioned near the boundary of the CRU. We were not able to establish a statistically significant difference with respect to spark morphology or frequency between the two models of NCX distribution, so we chose the interspersed distribution on the left as default.

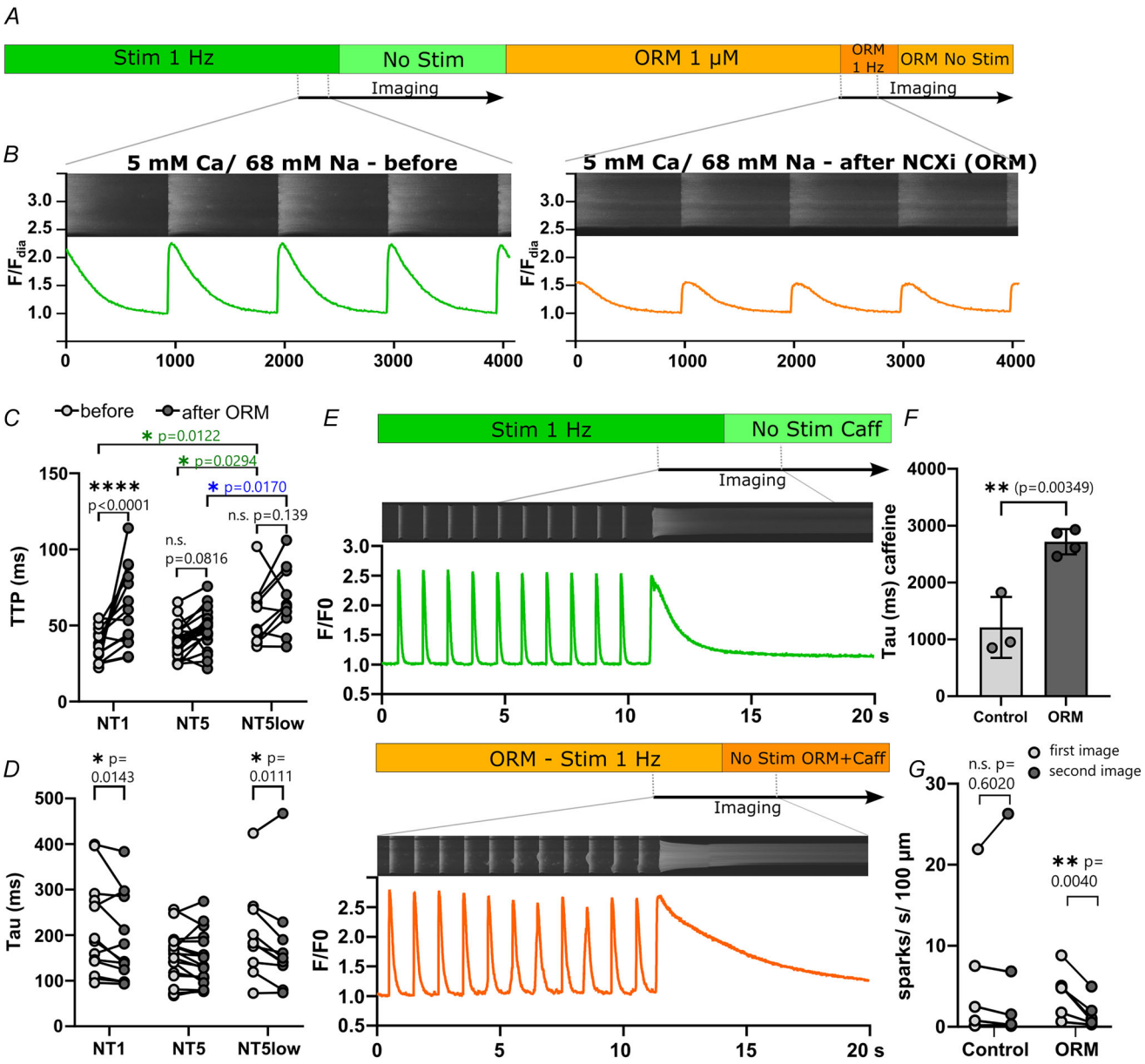

Figure A5. Calcium handling during NCX inhibition
Representative calcium transient before and during ORM treatment in 5 mM calcium solution with reduced sodium (NT5low *A*, *B*). Time-to-peak (TTP, *C*) and the time constant of calcium decay (Tau, *D*) during stimulation at 1 Hz. *E*, cardiomyocytes were transfused with 30 mM caffeine after stimulation without (upper panel) and with (lower panel) Na^+/Ca^{2+} exchanger (NCX) inhibition. Since calcium decay depends mostly on NCX during caffeine treatment, the time constant of decay (Tau, *F*) is significantly increased under simultaneous NCX inhibition. *G*, control experiments (in NT5, $n = 6$) with the same protocol, but without the addition of ORM before and during the second round of imaging did not show the same decrease in spark frequency. $^*P < 0.05$, $^{**}P < 0.01$, $^{***}P < 0.001$, $^{****}P < 0.0001$ per cell ($n = 16$ for NT1, $n = 20$ for NT5 and $n = 10$ for NT5low with four animals for *A*–*D* and $n = 3$–4 in one animal for *E* and *F*), tested with paired two-way ANOVA (*C*, *D*) or unpaired *t* test (*F*). Black asterisks indicate differences between before and with ORM, green asterisks between different buffers before ORM and blue asterisks between different buffers with ORM treatment.

References

Armoundas, A. A., Hobai, I. A., Tomaselli, G. F., Winslow, R. L., & O'Rourke, B. (2003). Role of sodium-calcium exchanger in modulating the action potential of ventricular myocytes from normal and failing hearts. *Circulation Research*, **93**(1), 46–53.

Aronsen, J. M., Swift, F., & Sejersted, O. M. (2013). Cardiac sodium transport and excitation–contraction coupling. *Journal of Molecular and Cellular Cardiology*, **61**, 11–19.

Barry, W. H. (2000). $Na^{(+)}$-$Ca^{(2+)}$ exchange in failing myocardium: Friend or foe? *Circulation Research*, **87**(7), 529–531.

Bentele, K., & Falcke, M. (2007). Quasi-steady approximation for ion channel currents. *Biophysical Journal*, **93**(8), 2597–608.

Bers, D. M., & Shannon, T. R. (2013). Calcium movements inside the sarcoplasmic reticulum of cardiac myocytes. *Journal of Molecular and Cellular Cardiology*, **58**, 59–66.

Blaustein, M. P., & Lederer, W. J. (1999). Sodium/calcium exchange: Its physiological implications. *Physiological Reviews*, **79**(3), 763–854.

Bouchard, R. A., Clark, R. B., & Giles, W. R. (1993). Role of sodium-calcium exchange in activation of contraction in rat ventricle. *The Journal of Physiology*, **472**, 391–413.

Brochet, D. X., Yang, D., Di Maio, A., Lederer, W. J., Franzini-Armstrong, C., & Cheng, H. (2005). Ca^{2+} blinks: Rapid nanoscopic store calcium signaling. *Proceedings of the National Academy of Sciences of the United States of America*, **102**(8), 3099–3104.

Cannell, M. B., Kong, C. H. T., Imtiaz, M. S., & Laver, D. R. (2013). Control of sarcoplasmic reticulum Ca^{2+} release by stochastic RyR gating within a 3D model of the cardiac dyad and importance of induction decay for CICR termination. *Biophysical Journal*, **104**(10), 2149–2159.

Chamakuri, N., Neubert, W., Gilbert, S., Vierheller, J., Warnecke, G., & Falcke, M. (2018). Multiscale modeling and numerical simulation of calcium cycling in cardiac myocytes. *Multiscale Modeling & Simulation*, **16**(3), 1115–1145.

Colman, M. A. (2019). Arrhythmia mechanisms and spontaneous calcium release: Bi-directional coupling between re-entrant and focal excitation. *PLoS Computational Biology*, **15**(8), e1007260.

Conesa, D., Echebarria, B., Penaranda, A., Cantalapiedra, I. R., Shiferaw, Y., & Alvarez-Lacalle, E. (2020). Two-variable nullcline analysis of ionic general equilibrium predicts calcium homeostasis in ventricular myocytes. *PloS Computational Biology*, **16**(6), e1007572.

Correia Pinto, J., Henriques-Coelho, T., Roncon-Albuquerque, R., Jr., & Leite-Moreira, A. F. (2006). Differential right and left ventricular diastolic tolerance to acute afterload and NCX gene expression in Wistar rats. *Physiological Research*, **55**(5), 513–526.

Cosi, F. G., Giese, W., Neubert, W., Luther, S., Chamakuri, N., Parlitz, U., & Falcke, M. (2019). Multiscale modeling of dyadic structure-function relation in ventricular cardiac myocytes. *Biophysical Journal*, **117**(12), 2409–2419.

De Angelis, A., Cappetta, D., Piegari, E., Rinaldi, B., Ciuffreda, L. P., Esposito, G., Ferraiolo, F. A., Rivellino, A., Russo, R., Donniacuo, M., Rossi, F., Urbanek, K., & Berrino, L. (2016). Long-term administration of ranolazine attenuates diastolic dysfunction and adverse myocardial remodeling in a model of heart failure with preserved ejection fraction. *International Journal of Cardiology*, **217**, 69–79.

Ferrier, G. R., Smith, R. H., & Howlett, S. E. (2003). Calcium sparks in mouse ventricular myocytes at physiological temperature. *American Journal of Physiology-Heart and Circulatory Physiology*, **285**(4), H1495–1505.

Ford, K. L., Moorhouse, E. L., Bortolozzi, M., Richards, M. A., Swietach, P., & Vaughan-Jones, R. D. (2017). Regional acidosis locally inhibits but remotely stimulates Ca^{2+} waves in ventricular myocytes. *Cardiovascular Research*, **113**(8), 984–995.

Gaughan, J. P., Furukawa, S., Jeevanandam, V., Hefner, C. A., Kubo, H., Margulies, K. B., McGowan, B. S., Mattiello, J. A., Dipla, K., Piacentino, V., 3rd, Li, S., & Houser, S. R. (1999). Sodium/calcium exchange contributes to contraction and relaxation in failed human ventricular myocytes. *American Journal of Physiology*, **277**(2), H714–H724.

Gilles, J. F., Dos Santos, M., Boudier, T., Bolte, S., & Heck, N. (2017). DiAna, an ImageJ tool for object-based 3D co-localization and distance analysis. *Methods (San Diego, Calif.)*, **115**, 55–64.

Gomez, A. M., Valdivia, H. H., Cheng, H., Lederer, M. R., Santana, L. F., Cannell, M. B., McCune, S. A., Altschuld, R. A., & Lederer, W. J. (1997). Defective excitation-contraction coupling in experimental cardiac hypertrophy and heart failure. *Science*, **276**(5313), 800–806.

Hake, J., Edwards, A. G., Yu, Z., Kekenes-Huskey, P. M., Michailova, A. P., McCammon, J. A., Holst, M. J., Hoshijima, M., & McCulloch, A. D. (2012). Modelling cardiac calcium sparks in a three-dimensional reconstruction of a calcium release unit. *The Journal of physiology*, **590**(18), 4403–4422.

Heinzel, F. R., Bito, V., Volders, P. G., Antoons, G., Mubagwa, K., & Sipido, K. R. (2002). Spatial and temporal inhomogeneities during Ca^{2+} release from the sarcoplasmic reticulum in pig ventricular myocytes. *Circulation Research*, **91**(11), 1023–1030.

Higgins, E. R., Goel, P., Puglisi, J. L., Bers, D. M., Cannell, M., & Sneyd, J. (2007). Modelling calcium microdomains using homogenisation. *Journal of Theoretical Biology*, **247**(4), 623–644.

Jayasinghe, I., Cannell, M. B., & Soeller, C. (2009). Organization of ryanodine receptors, transverse tubules, and sodium-calcium exchanger in rat myocytes. *Biophysical Journal*, **97**(10), 2664–2673.

Jayasinghe, I., Clowsley, A. H., Lin, R., Lutz, T., Harrison, C., Green, E., Baddeley, D., Di Michele, L., & Soeller, C. (2018). True molecular scale visualization of variable clustering properties of Ryanodine receptors. *Cell Reports*, **22**(2), 557–567.

Kamimura, D., Ohtani, T., Sakata, Y., Mano, T., Takeda, Y., Tamaki, S., Omori, Y., Tsukamoto, Y., Furutani, K., Komiyama, Y., Yoshika, M., Takahashi, H., Matsuda, T., Baba, A., Umemura, S., Miwa, T., Komuro, I., & Yamamoto, K. (2012). Ca^{2+} entry mode of Na^{+}/Ca^{2+} exchanger as a new therapeutic target for heart failure with preserved ejection fraction. *European Heart Journal*, **33**(11), 1408–1416.

Landstrom, A. P., Dobrev, D., & Wehrens, X. H. T. (2017). Calcium signaling and cardiac arrhythmias. *Circulation Research*, **120**(12), 1969–1993.

Langer, G. A., & Peskoff, A. (1997). Role of the diadic cleft in myocardial contractile control. *Circulation*, **96**(10), 3761–3765.

Larbig, R., Torres, N., Bridge, J. H., Goldhaber, J. I., & Philipson, K. D. (2010). Activation of reverse Na^+-Ca^{2+} exchange by the Na^+ current augments the cardiac Ca^{2+} transient: Evidence from NCX knockout mice. *The Journal of Physiology*, **588**(Pt 17), 3267–3276.

Li, S. Z., Wu, F., Wang, B., Wei, G. Z., Jin, Z. X., Zang, Y. M., Zhou, J. J., & Wong, T. M. (2007). Role of reverse mode Na^+/Ca^{2+} exchanger in the cardioprotection of metabolic inhibition preconditioning in rat ventricular myocytes. *European Journal of Pharmacology*, **561**(1–3), 14–22.

Lines, G. T., Sande, J. B., Louch, W. E., Mork, H. K., Grottum, P., & Sejersted, O. M. (2006). Contribution of the Na^+/Ca^{2+} exchanger to rapid Ca^{2+} release in cardiomyocytes. *Biophysical Journal*, **91**(3), 779–792.

Maltsev, A. V., Ventura Subirachs, V., Monfredi, O., Juhaszova, M., Ajay Warrier, P., Rakshit, S., Tagirova, S., Maltsev, A. V., Stern, M. D., Lakatta, E. G., & Maltsev, V. A. (2024). Structure-function relationship of the ryanodine receptor cluster network in sinoatrial node cells. *Cells*, **13**(22), 1885.

Moench, I., & Lopatin, A. N. (2014). $Ca^{(2+)}$ homeostasis in sealed t-tubules of mouse ventricular myocytes. *Journal of Molecular and Cellular Cardiology*, **72**, 374–383.

Neubert, W., Falcke, M., & Chamakuri, N. (2026). Multiscale simulation and parallel space–time adaptivity of calcium sparks in cardiac myocytes. *Computer Methods and Programs in Biomedicine*, **274**, 109154.

Nivala, M., Ko, C. Y., Nivala, M., Weiss, J. N., & Qu, Z. (2013). The emergence of subcellular pacemaker sites for calcium waves and oscillations. *The Journal of Physiology*, **591**(21), 5305–5320.

Ottolia, M., Torres, N., Bridge, J. H., Philipson, K. D., & Goldhaber, J. I. (2013). Na/Ca exchange and contraction of the heart. *Journal of Molecular and Cellular Cardiology*, **61**, 28–33.

Primessnig, U., Bracic, T., Levijoki, J., Otsomaa, L., Pollesello, P., Falcke, M., Pieske, B., & Heinzel, F. R. (2019). Long-term effects of $Na^{(+)}$ /$Ca^{(2+)}$ exchanger inhibition with ORM-11035 improves cardiac function and remodelling without lowering blood pressure in a model of heart failure with preserved ejection fraction. *European Journal of Heart Failure*, **21**(12), 1543–1552.

Primessnig, U., Schonleitner, P., Holl, A., Pfeiffer, S., Bracic, T., Rau, T., Kapl, M., Stojakovic, T., Glasnov, T., Leineweber, K., Wakula, P., Antoons, G., Pieske, B., & Heinzel, F. R. (2016). Novel pathomechanisms of cardiomyocyte dysfunction in a model of heart failure with preserved ejection fraction. *European Journal of Heart Failure*, **18**(8), 987–997.

Rouhana, S., Farah, C., Roy, J., Finan, A., Rodrigues de Araujo, G., Bideaux, P., Scheuermann, V., Saliba, Y., Reboul, C., Cazorla, O., Aimond, F., Richard, S., Thireau, J., & Fares, N. (2019). Early calcium handling imbalance in pressure overload-induced heart failure with nearly normal left ventricular ejection fraction. *Biochimica Et Biophysica Acta Molecular Basis of Disease*, **1865**(1), 230–242.

Sato, D., Despa, S., & Bers, D. M. (2012). Can the sodium-calcium exchanger initiate or suppress calcium sparks in cardiac myocytes? *Biophysical Journal*, **102**(8), L31–L33.

Schendel, T., Thul, R., Sneyd, J., & Falcke, M. (2012). How does the ryanodine receptor in the ventricular myocyte wake up: By a single or by multiple open L-type Ca^{2+} channels? *European Biophysics Journal*, **41**(1), 27–39.

Semmler, L., Jeising, T., Huettemeister, J., Bathe-Peters, M., Georgoula, K., Roshanbin, R., Sander, P., Fu, S., Bode, D., Hohendanner, F., Pieske, B., Annibale, P., Schiattarella, G. G., Oeing, C. U., & Heinzel, F. R. (2024). Impairment of the adrenergic reserve associated with exercise intolerance in a murine model of heart failure with preserved ejection fraction. *Acta Physiologica (Oxford, England)*, **240**(4), e14124.

Setterberg, I. E., Le, C., Frisk, M., Li, J., & Louch, W. E. (2021). The physiology and pathophysiology of T-tubules in the heart. *Frontiers in Physiology*, **12**, 718404.

Shannon, T. R., Wang, F., Puglisi, J., Weber, C., & Bers, D. M. (2004). A mathematical treatment of integrated Ca dynamics within the ventricular myocyte. *Biophysical Journal*, **87**(5), 3351–3371.

Sheard, T. M. D., Hurley, M. E., Colyer, J., White, E., Norman, R., Pervolaraki, E., Narayanasamy, K. K., Hou, Y., Kirton, H. M., Yang, Z., Hunter, L., Shim, J.-u., Clowsley, A. H., Smith, A. J., Baddeley, D., Soeller, C., Colman, M. A., & Jayasinghe, I. (2019). Three-dimensional and chemical mapping of intracellular signaling nanodomains in health and disease with enhanced expansion microscopy. *ACS Nano*, **13**(2), 2143–2157.

Shepherd, N., & McDonough, H. B. (1998). Ionic diffusion in transverse tubules of cardiac ventricular myocytes. *American Journal of Physiology*, **275**(3), H852–H860.

Sher, A. A., Noble, P. J., Hinch, R., Gavaghan, D. J., & Noble, D. (2008). The role of the Na^+/Ca^{2+} exchangers in Ca^{2+} dynamics in ventricular myocytes. *Progress in Biophysics and Molecular Biology*, **96**(1), 377–398.

Shiferaw, Y., Aistrup, G. L., Louch, W. E., & Wasserstrom, J. A. (2020). Remodeling promotes proarrhythmic disruption of calcium homeostasis in failing atrial myocytes. *Biophysical Journal*, **118**(2), 476–491.

Shiferaw, Y., Aistrup, G. L., & Wasserstrom, J. A. (2017). Mechanism for triggered waves in atrial myocytes. *Biophysical Journal*, **113**(3), 656–670.

Soeller, C., & Cannell, M. B. (1997). Numerical simulation of local calcium movements during L-type calcium channel gating in the cardiac diad. *Biophysical Journal*, **73**(1), 97–111.

Stern, M. D., Song, L.-S., Cheng, H., Sham, J. S. K., Yang, H. T., Boheler, K. R., & Rios, E. (1999). Local control models of cardiac excitation-contraction coupling. A possible role for allosteric interactions between ryanodine receptors. *Journal of General Physiology*, **113**(3), 469–489.

Stevenson-Cocks, H. (2019). Biophysical *modelling of rat cardiac electrophysiology and calcium han*dling [PhD Thesis, The University of Leeds].

Subramanian, S., Viatchenko-Karpinski, S., Lukyanenko, V., Gyorke, S., & Wiesner, T. F. (2001). Underlying mechanisms of symmetric calcium wave propagation in rat ventricular myocytes. *Biophysical Journal*, **80**(1), 1–11.

Tanaka, H., Shimada, H., Namekata, I., Kawanishi, T., Iida-Tanaka, N., & Shigenobu, K. (2007). Involvement of the Na^+/Ca^{2+} exchanger in ouabain-induced inotropy and arrhythmogenesis in guinea-pig myocardium as revealed by SEA0400. *Journal of Pharmacological Sciences*, **103**(2), 241–246.

Toth, N., Loewe, A., Szlovak, J., Kohajda, Z., Bitay, G., Levijoki, J., Papp, J. G., Varro, A., & Nagy, N. (2022). The reverse mode of the $Na^{(+)}/Ca^{(2+)}$ exchanger contributes to the pacemaker mechanism in rabbit sinus node cells. *Scientific Reports*, **12**(1), 21830.

Tykocki, N. R., Jackson, W. F., & Watts, S. W. (2012). Reverse-mode Na^+/Ca^{2+} exchange is an important mediator of venous contraction. *Pharmacological Research*, **66**(6), 544–554.

Vermij, S. H., Abriel, H., & Kucera, J. P. (2019). Modeling depolarization delay, sodium currents, and electrical potentials in cardiac transverse tubules. *Frontiers in Physiology*, **10**, 1487.

Vierheller, J., Neubert, W., Falcke, M., Gilbert, S. H., & Chamakuri, N. (2015). A multiscale computational model of spatially resolved calcium cycling in cardiac myocytes: From detailed cleft dynamics to the whole cell concentration profiles. *Frontiers in Physiology*, **6**, 255.

Walker, M. A., Williams, G. S. B., Kohl, T., Lehnart, S. E., Jafri, M. S., Greenstein, J. L., Lederer, W. J., & Winslow, R. L. (2014). Superresolution modeling of calcium release in the heart. *Biophysical Journal*, **107**(12), 3018–3029.

Zhang, X., Ni, H., Morotti, S., Smith, C. E. R., Sato, D., Louch, W. E., Edwards, A. G., & Grandi, E. (2023). Mechanisms of spontaneous Ca^{2+} release-mediated arrhythmia in a novel 3D human atrial myocyte model: I. Transverse-axial tubule variation. *The Journal of Physiology*, **601**(13), 2655–2683.

Zhang, X., Smith, C. E., Morotti, S., Edwards, A. G., Sato, D., Louch, W. E., Ni, H., & Grandi, E. (2023). Mechanisms of spontaneous Ca^{2+} release-mediated arrhythmia in a novel 3D human atrial myocyte model: II. Ca^{2+}-handling protein variation. *The Journal of physiology*, **601**(13), 2685–2710.

Zhao, Z., Gordan, R., Wen, H., Fefelova, N., Zang, W. J., & Xie, L. H. (2013). Modulation of intracellular calcium waves and triggered activities by mitochondrial ca flux in mouse cardiomyocytes. *PLoS ONE*, **8**(11), e80574.

Additional information

Data availability statement

All data supporting the results are either included in the paper itself or included in Table 'Data set' in the online supporting information.

Competing interests

None of the authors reports perceived or potential conflict of interest, financial or otherwise.

Author contributions

Conception or design of the work: W.N., J.H., P.S., N.C., F.H., F.R.H., M.F. Acquisition, analysis or interpretation of data for the work: W.N., J.H., P.S., N.C., F.R.H., M.F. Drafting the work or revising it critically for important intellectual content: W.N., J.H., P.S., N.C., F.H., F.R.H., M.F.

Funding

This work was funded by the Deutsche Forschungsgemeinschaft (DFG) under project number FA 350/17-1 to MF and HE 7737/4-1 to FRH.

Acknowledgements

We thank PD Dr Jörg Piontek for support with the STED imaging and Gabriele Boehm for technical support.

Keywords

cardiac myocytes, diastolic dysfunction, excitation–contraction coupling, Na^+/Ca^{2+} exchanger

Supporting information

Additional supporting information can be found online in the Supporting Information section at the end of the HTML view of the article. Supporting information files available:

Peer review history
Supplemtary information